remote sensing

MDPI

Article

Characterizing the Patterns and Trends of Urban Growth in Saudi Arabia's 13 Capital Cities Using a Landsat Time Series

Amal H. Aljaddani [1,2,*], Xiao-Peng Song [1] and Zhe Zhu [3]

[1] Department of Geosciences, Texas Tech University, Lubbock, TX 79409, USA; xiaopeng.song@ttu.edu
[2] Department of Geographic Information System, College of Social Sciences, University of Jeddah, Jeddah 21589, Saudi Arabia
[3] Department of Natural Resources and the Environment, University of Connecticut, Storrs, CT 06269, USA; zhe@uconn.edu
* Correspondence: amal.h.aljaddani@ttu.edu or ahaljaddani@uj.edu.sa

Abstract: Development and a growing population in Saudi Arabia have led to a substantial increase in the size of its urban areas. This sustained development has increased policymakers' need for reliable data and analysis regarding the patterns and trends of urban expansion throughout the country. Although previous studies on urban growth in Saudi cities exist, there has been no comprehensive research that focused on all 13 regional capitals within the country. Our study addressed this gap by producing a new annual long-term dataset of 30 m spatial resolution that covered 35 years (1985–2019) and maintained a high overall accuracy of annual classifications across the study period, ranging between 93 and 98%. Utilizing the continuous change detection and classification (CCDC) algorithm and all available Landsat data, we classified Landsat pixels into urban and non-urban classes with an annual frequency and quantified urban land cover change over these 35 years. We implemented a stratified random sampling design to assess the accuracy of the annual classifications and the multi-temporal urban change. The results revealed that Saudi capitals experienced massive urban growth, from 1305.28 ± 348.71 km^2 in 1985 to 2704.94 ± 554.04 km^2 in 2019 (± values represent the 95% confidence intervals). In addition to the high accuracy of the annual classifications, the overall accuracy of the multi-temporal urban change map was also high and reached 91%. The urban expansion patterns varied from city to city and from year to year. Most capital cities showed clear growth patterns of edge development, that is, a continuous expansion of built-up lands radiating from existing urban areas. This study provides distinct insights into the urban expansion characteristics of each city in Saudi Arabia and a synoptic view of the country as a whole over the past four decades. Our results provided a dataset that can be used as the foundation for future socioeconomic and environmental studies.

Keywords: CCDC; urban growth; time series; Landsat; stratified sampling; land use and land cover change; Saudi Arabia

Citation: Aljaddani, A.H.; Song, X.-P.; Zhu, Z. Characterizing the Patterns and Trends of Urban Growth in Saudi Arabia's 13 Capital Cities Using a Landsat Time Series. *Remote Sens.* **2022**, *14*, 2382. https://doi.org/10.3390/rs14102382

Academic Editor: Xuan Zhu

Received: 15 April 2022
Accepted: 12 May 2022
Published: 15 May 2022

1. Introduction

The world's population reached nearly 7.5 billion in 2017 and is projected to grow to 10.2 billion by 2050 [1]. Though urban areas encompass only a small fraction of the Earth's total land surface [2], most of the population growth in the predictable future will occur in urban areas [3,4]. According to the literature, future increases in urban expansion will mostly occur in small and medium-sized cities [5–7]. Even though urban areas are central to wealth and economic development, generating more than 70% of the world's gross domestic product (GDP) [8], they are considered one of the most significant drivers of various aspects of global change, such as the loss of agriculture, deforestation, habitat degradation, and pollution [9–15]. Hence, having accurate information about urban

expansion and its spatial distribution is key for scientists and policymakers to understand the causes and consequences of urban expansion.

Satellite remote sensing (RS) can provide synoptic and consistent measurements of the Earth's surface, generating reliable urban land cover maps in different geographical locations. Numerous urban land cover studies have focused on mapping urban land cover at global scales using a coarse spatial resolution with a high temporal frequency, such as the Moderate Resolution Imaging Spectroradiometer (MODIS). A recent study by Buchhorn et al. (2021) [16] generated annual land use and land cover maps globally between 2015 and 2019 using the MODIS at 100 m. This research produced maps annually, each of which was distinctive and detailed 23-classification levels based on the Land Cover Classification System (LCCS). The overall accuracy of this study was 80.6% in 2015 and 80.3% in 2019. Another study by Huang et al. (2021) [17] generated a 250 m MODIS global urban extent product (MGUP) from 2001 to 2018 using an automated mapping approach. The accuracy assessment of this research achieved better results, with an F-score of 0.88, than other products, such as the MODIS Land Cover Type product (MCD12Q1.v5 and MCD12Q1.v6), which were 0.82 and 0.86, respectively [18,19]. This research found that urban expansion grew to 802,233 km^2, which represented 0.54% of the Earth's surface. The research also showed that urban areas expanded globally by 1.68 times between 2001 and 2018.

While some studies have focused on mapping the global extent of urban areas using MODIS, nighttime light studies have relied on light output to distinguish global urban extent. For instance, Zhou et al. (2015) [20] implemented a cluster-based method using the defense meteorological satellite program/operational linescan system nighttime stable-light data (DMSP/OLS NTL). This study generated a new global map of the urban extent at a 1 km spatial resolution in 2000. According to this research, the overall accuracy was 87%, producer accuracy was 96%, and user accuracy was 88%. Zhou et al. (2015) indicated that the results of mapping urban areas had shown a high degree of achievement compared with other products, such as MODIS 500 m, GlobCover, GLC2000, Global Land Cover 2000 (GLC2000), Global Rural-Urban Mapping Project (GRUMP), and NOAA's impervious surface area map (IMPSA) [21–25].

Global urban studies that use satellites with coarser spatial resolutions have a limited capability for capturing small and detailed urban land cover changes. However, this is not the only reason for researchers to switch to satellites with finer spatial resolutions, as the availability of data is another important benefit of satellites with these capabilities. Accordingly, many recent urban studies have shifted to satellites with a resolution of 5–100 m/pixel, such as Landsat and the Sentinel. For example, the Global Human Settlement Layer (GHSL) is a global urban product comprised of three levels of mapping: built-up, population density, and settlement. These levels were produced in four specified epochs—1975, 1990, 2000, and 2014. Varied input data have been used to produce a GHSL, including satellite imagery, demographic data, and volunteer geographic information systems. The finer spatial resolution of Landsat and Sentinel satellite imagery was used for mapping the built-up areas [26]. Seminal contributions to this shift were been made by Small (2005) [27], who employed a spectral mixture analysis (SMA) approach using the Landsat-7 Enhanced Thematic Mapper Plus (ETM+) between 1999 and 2003 for a set of 28 urban areas globally. This study exhibited a spectral description of urban reflectance properties that showed the reflectance of the urban areas could be precisely explained as a linear combination of three spectral endmembers: high-albedo, dark albedo, and vegetation. The urban areas can be distinguished near the dark side of the mixing line between high and dark albedo endmembers.

A study conducted by Gong et al. (2020) [28] produced a Global Artificial Impervious Areas (GAIA) covering more than 30 years using 30-m spatial resolution Landsat images through the Google Earth Engine platform. This study included nighttime light data and the Sentinel-1 Synthetic Aperture Radar (SAR) data as ancillary datasets to improve the performance of their formerly developed algorithm in arid areas [29]. The overall accuracy

of GAIA products for 1985, 1990, 1995, 2000, 2005, 2010, and 2015 was higher than 90%. The resultant of GAIA products has increased to about 797,076 km^2 in 2018, which is 1.5 times greater than it was in 1990. The GAIA study focused on the ten countries with the greatest percentage of artificial impervious area, indicating that China and the United States (US) were the top two, respectively. Hence, the finer spatial resolution datasets have made it possible to collect detailed information about urban growth in different geographical locations. Despite the availability of some higher spatial resolution satellite imagery that can monitor particular Earth surfaces at specific times, the only imagery with a long temporal record is that of Landsat. This data is of particular use to researchers, as it has captured changes on the Earth's surfaces since 1972.

This shift towards measuring urban growth using Landsat can be of particular use in monitoring countries that have experienced rapid economic growth and increases in population, such as Saudi Arabia. Between 1974 and 2019, Saudi Arabia's population jumped from just over 7 million to almost 35 million, an increase of nearly 500% [30]. In addition, Saudi Arabia is the largest petroleum producer in the world, accounting for 19% of global reserves, 12% of global production, and more than 20% of petroleum sales in the global market [31]. As such, the petroleum industry has heavily influenced the growth of the country's economy [32], which has, in turn, stimulated rapid urban growth in populated regions. Despite these increases, studies dedicated to analyzing urban growth in Saudi cities are relatively few, though there have been notable exceptions that have employed various approaches and focused on either individual cities or small groups of cities. Abdelatti et al. (2017) [33] examined urban growth in the Alahsa province in Saudi Arabia and relied on reports, statistical data, and periodicals from vetted sources as well as reports produced by the General Authority for Statistics in Saudi Arabia. The results showed an increase in urban areas in the province, which climbed from 76.49 km^2 in 1992 to 91.62 km^2 in 2011. Alhowaish (2015) [34] studied the urban growth of the metropolitan area in Dammam over eight decades based on socioeconomic reports and statistical data from different agencies in Saudi Arabia. Al-Shihri (2016) [35] examined the influence of large-scale residential development projects on urban sustainability in the Dammam metropolitan area (DMA) and recommended that the boundaries of the DMA's shorelines be accurately delineated and that a strict prohibition of further development is enforced in these areas in order to minimize the impact of unsustainable growth. Aljoufie (2013) [36] developed eight indices related to urban growth and transportation changes and then used RS and a geographic information system (GIS) to analyze urban growth in Jeddah, Saudi Arabia, a city that witnessed rapid growth between 1964 and 2007. Jamali and Rahman (2016) [37] examined urban growth in Riyadh, Saudi Arabia, using RS and a GIS on Landsat images in 1990, 2000, and 2014 and were able to provide recommendations for sustainable growth in the city. Aljaddani (2015) [38] was able to detect land cover and land use changes in the city of Jeddah utilizing RS and GIS. Landsat images in 1984, 2000, and 2013 were analyzed and the study showed that Jeddah had witnessed rapid growth over the study period and was expected to increase over the coming years.

Much of the research conducted regarding urban growth has overlooked Saudi Arabia. Global studies have, of course, included distinctive information on the country's cities; however, as these studies are globally focused, they utilize a coarse spatial resolution or a fine spatial resolution with specified epochs [16,17,20,26]. Studies conducted locally have provided valuable information about urban growth using a variety of approaches and data; however, they were limited in that they addressed only one city, province, or metropolitan area and relied on statistical data, periodicals from vetted sources, or a few satellite images from different dates [33–38]. This lack of attention to urban growth in Saudi Arabia's cities at a detailed level over a sustained period of time represents a gap in current literature and a hindrance to local politicians and policymakers who lack the most detailed information on urban growth in the country. The purpose of this study is to address this need by producing a new long-term dataset at a spatial resolution of 30 m that details the distributions, heterogeneities, and dynamics of the rapid

growth that has occurred in the country's 13 capital cities. We conducted a time series analysis using the continuous change detection and classification (CCDC) algorithm for each city utilizing all available Landsat images over the past 35 years and aimed to answer the following question: What were these cities' urban growth patterns and trends between 1985 and 2019?

2. Study Area and Methods

2.1. Study Area

Saudi Arabia is located in Southwest Asia and occupies about four-fifths of the Arabian Peninsula. The total landmass of the kingdom is about 2,149,690 km^2, and the country's total population as of 2020 was 35,013,414 [39,40]. This number represents about 65.1% of the total population in the Gulf Cooperation Council (GCC) [41].

Saudi Arabia is composed of 13 administrative regions, and each region has a capital city. This research was focused on these 13 capitals: Riyadh (which also serves as the country's capital), Buridah, Ha'il, Dammam, Makkah, Madinah, Arar, Skakah, Tabuk, Albaha, Abha, Jazan, and Najran (Figure 1). Each city was assigned boundaries based on the 2019 Saudi Geological Survey (SGS) [42]. Riyadh and Buridah are located in the center of Saudi Arabia, and Ha'il is located to the northwest of Buridah city. These three cities are surrounded by the Al-Dahnā desert to the east, as well as dried valleys that exist throughout the central regions. In addition, there are several oases that are relatively close to Buridah. The city of Dammam is located in the eastern region of the country, overlooking the Arabia (Persian) Gulf. The eastern region is dominated by the Rub' al Khali desert, also known as the Empty Quarter, which covers 650,000 km^2 [43]. There are also several oases/cities that exist in the region [44]. Cities that are located in the western portions of Saudi Arabia, such as Madinah, Makkah, and Albaha, are located in the Sarwat Mountain series, and most of these cities also overlook the Red Sea to their west. The north and northwest regions in Saudi Arabia are known for fertile pasture and agriculture areas, and they are where Arar, Skakah, and Tabuk are located. Abha, Jazan, and Najran are located in the country's southwestern region near the Red Sea, a region that is home to the second-highest peak in the country, namely, the Sawda mountains (3000 m) [45]. These three cities are characterized by fertile agricultural areas and distinct topographic features. Overall, due to arid lands, the climate is generally dry, hot in the summer, and mild-to-cold in the winter with little rainfall [46].

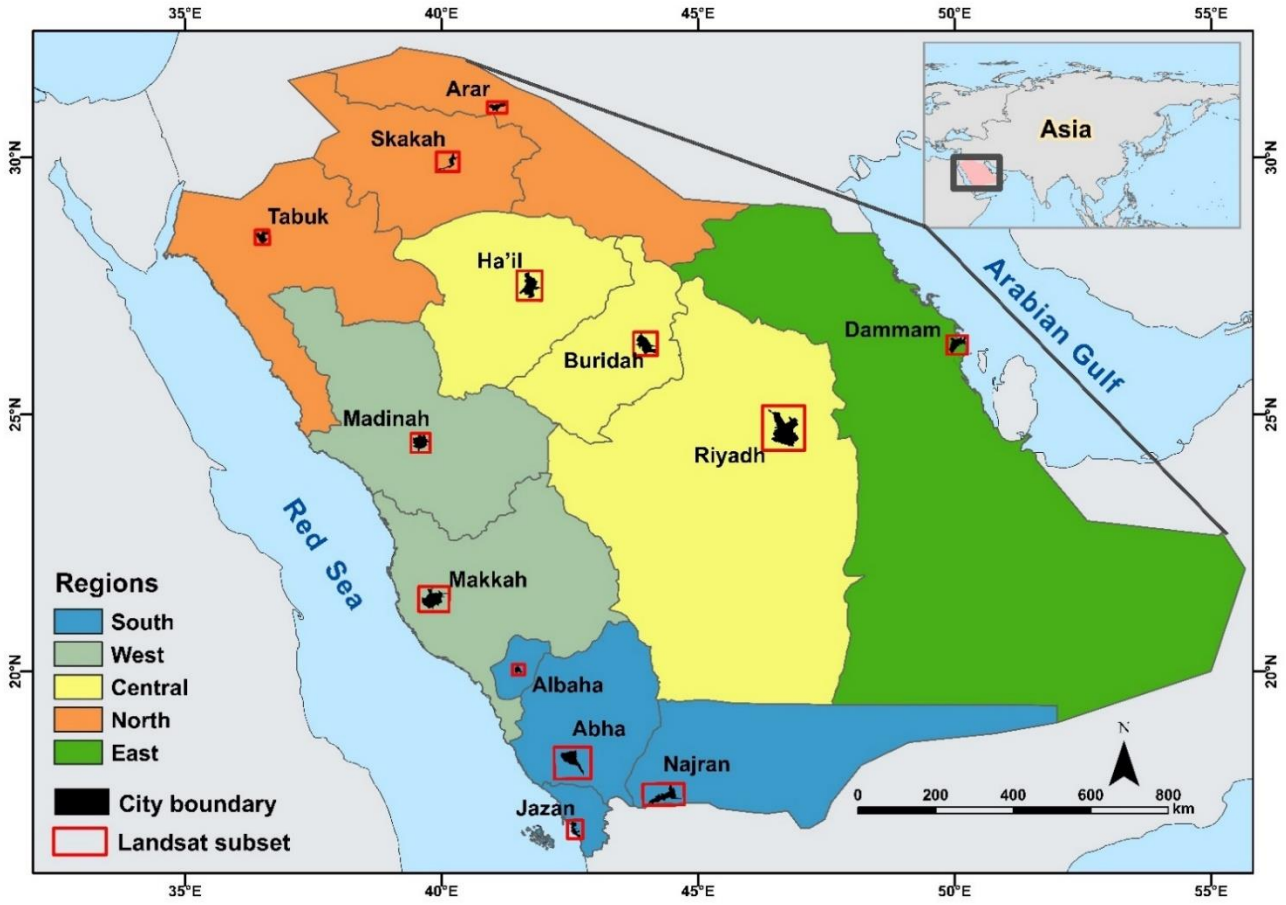

Figure 1. The 13 regions in Saudi Arabia and the geographic location of each region's capital. The red squares/rectangles represent the subsets of Landsat boundaries that were employed in this research. The asymmetric black represents the boundary of each city.

2.2. Landsat Data

The CCDC algorithm relies on geometric registration and atmospheric correction, which facilitates the comparison of images over time. For this study, we downloaded all Landsat level 1 surface reflectance data from the U.S. Geological Survey website [47], as the data are registered accurately. The data includes Landsat data from the Thematic Mapper 4-5 (TM), Enhanced Thematic Mapper Plus 7 (ETM+), and Operational Land Imager 8 (OLI) from 1985 to 2019. These data on the website are preprocessed using the Landsat Ecosystem Disturbance Adaptive Processing System (LEDAPS), which conducts atmospheric corrections [48,49]. To achieve these corrections, LEDAPS produces the surface reflectance products from the Landsat Thematic Mapper (TM 4-5) and Enhanced Thematic Mapper (ETM+ 7). The Landsat 8 Surface Reflectance system (L8SR) produces the surface reflectance products from the Landsat Operational Land Imager [50,51]. These datasets use a Worldwide Reference System (WRS-2) with a clear observation for more than 20% of Landsat images. The "clear" observations are defined as observations that are not obscured by cloud or cloud shadow or have snow detected based on the QA band derived from the Fmask algorithm [52,53]. In total, 15,922 preprocessed Landsat images were downloaded (Figure 2).

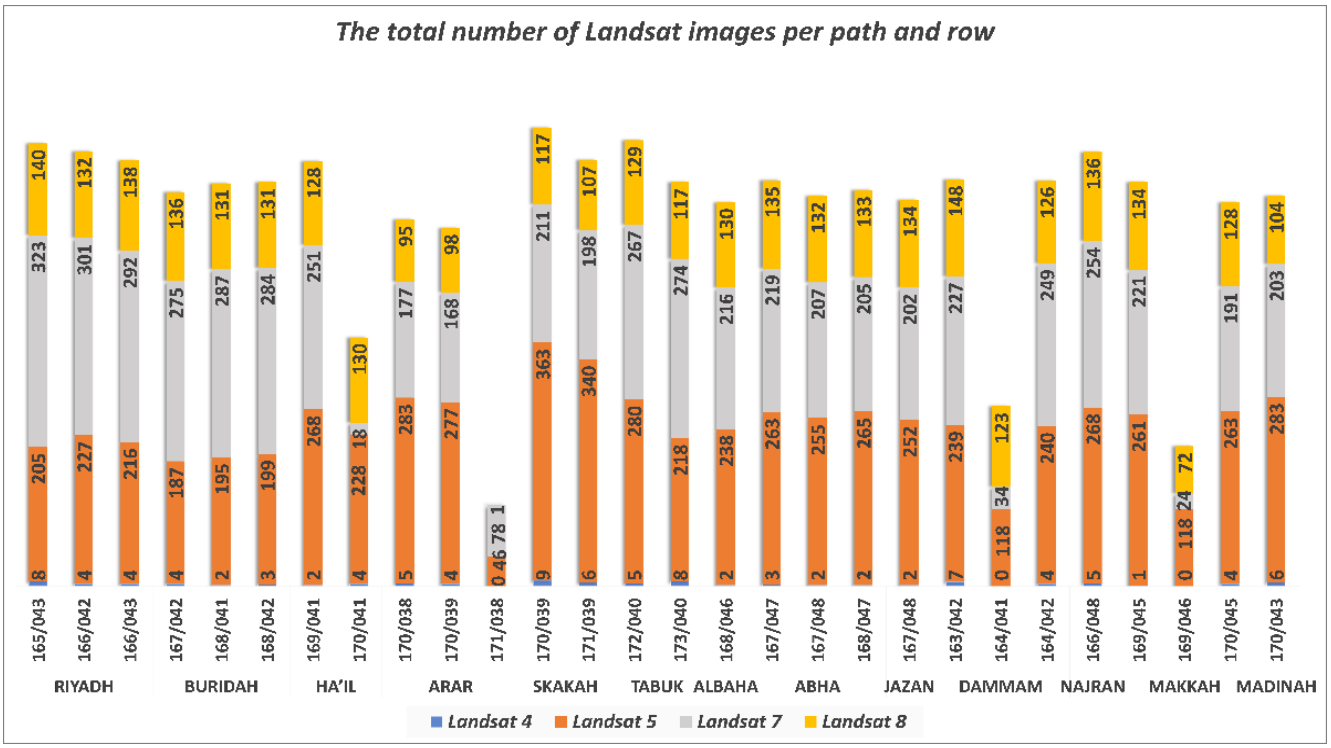

Figure 2. The total number of Landsat images per path and row for each capital (1985–2019).

3. Data Processing

We used the CCDC method to analyze the urban growth of the Saudi capitals. This approach included the following components: training data, a CCDC algorithm for continuous urban classification, estimating the accuracy and unbiased area, and estimating urban expansion rate and intensity (1985–2019).

3.1. Training Data

The land use and land cover training dataset was restricted to the period that is covered by the Landsat imagery to train the CCDC algorithm [54,55]. The training samples were collected between 2002 and 2015. Due to the limited pixels of some land use and land cover classes, ensuring that there were sufficient training samples per class became the primary goal during the Landsat satellite imagery selection process. We collected the training samples using Landsat satellite imagery and compared them with historically higher spatial resolution aerial imagery from Google Earth, and when there was obscurity, we assigned them to Landsat imagery (Figure 3). Two classes of land use and land cover were used to collect the samples of training data based on the USGS scheme of Anderson's land classification [56]. The first of the two classes was urban areas (developed class), which consist of a high percentage of constructed materials (30% or greater). These samples included residential, commercial, and industrial areas, as well as transportation networks, communication sites, and utilities. The second class was non-urban area (other), referring to all land cover classes combined, including agricultural land, rangeland, shrublands, water, and barren land. Table 1 shows detailed information about the urban and non-urban pixels, city size, the collection dates, and the paths and rows included.

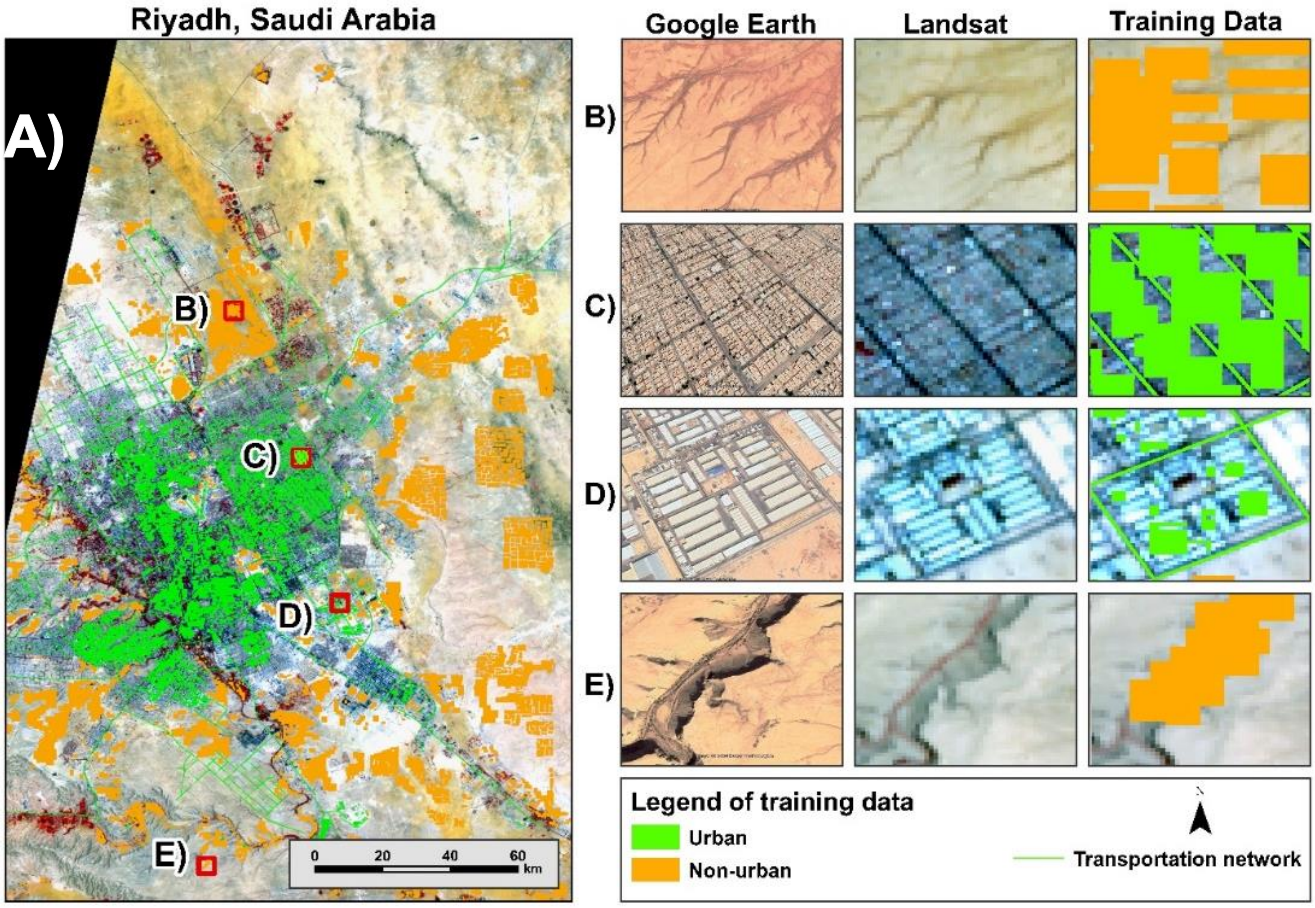

Figure 3. (**A**) Overview of Riyadh, Saudi Arabia. (**B**–**E**) Urban and non-urban training data at four different sites in Riyadh.

Table 1. Collected training data from the 13 capitals.

City Name	Urban Pixels	Non-Urban Pixels	City Size (km × km)	Date	Path/Row
Riyadh	232,609	534,025	83.49 × 97.74	2013	165/043
Buridah	76,259	1,327,780	47.34 × 50.37	2014	168/042
Ha'il	42,245	1,293,491	49.74 × 64.14	2005	169/041
Dammam	231,310	71,966	40.59 × 40.47	2014	163/042
Makkah	39,121	518,555	61.11 × 54.21	2013	169/045
Madinah	51,394	374,444	38.43 × 40.68	2005	170/043
Arar	11,461	352,432	37.05 × 25.5	2004	170/039
Skakah	15,566	730,318	43.08 × 42.84	2003	171/039
Tabuk	29,155	511,715	28.2 × 31.5	2005	173/040
Albaha	3054	91,936	25.32 × 23.52	2002	168/046
Abha	11,464	318,887	77.43 × 68.91	2013	167/047
Jazan	13,093	160,557	32.52 × 39.69	2010	167/048
Najran	45,726	953,402	86.25 × 45.33	2015	166/048
Total pixels	802,457	7,239,508			

3.2. CCDC Algorithm for Continuous Urban Classification

The CCDC algorithm was selected because it has the capability to continuously detect the land use and land cover changes and produce change detection and classification maps at any given time. The algorithm used all available Landsat satellite images to

estimate the time series model and used this model to predict future observations [54,55]. The time series model of the CCDC algorithm consists of three main components—seasonality, trend, and break—that can capture different types of changes to the Earth's surface, such as vegetation phenology, gradual change, and abrupt change (e.g., urbanization and deforestation). These three main components were used as coefficients in the time series model that analyzed the clear-sky observations. In this time series model, changes can be detected if the differences between the new observations are not within the prediction range for three consecutive observations. When this occurs, a break in the time series model is flagged. Once there is a break, the number of observations is increased, and a new time series model is estimated. If no change is found, a new clear-sky observation is added to the time series model, and it is estimated again. The break that is found in the time series provides change information. The coefficients of seasonality and trend and the root-mean-square error (RMSE) with the training samples are used as an input for the classification process that uses the random forest classifier (RFC) because it produces highly accurate predictions and efficiently computes large databases [57]. In this research, we fed the CCDC with the training data to produce the classification maps for the 13 capital cities in the first month of July across all of the years that were included in this study. We then accumulated the annual classification maps, which consisted of binary classes (urban and non-urban), to track and monitor changes in urban growth from 1985 to 2019.

3.3. Estimating the Accuracy and Unbiased Area

We implemented a stratified random sampling design, which allowed us to assess the accuracy of the annual classification maps and multi-temporal urban change map, as well as provide area estimations and uncertainties. The strata were defined based on the natural states of the classification map, which were divided into three main categories: "likely change," "stable urban," and "stable non-urban." We identified each stratum by employing a frequency map that was based on an overlay of all classification maps for each city from 1985 to 2019 (Figure 4). If a pixel on all 35 maps was classified as urban, it was included in the "stable urban" stratum. If a pixel on all 35 maps was classified as non-urban, it was included in the "stable non-urban" stratum. If a pixel on any of the 35 maps had changed from urban to non-urban or vice versa, it was included as "likely change." A frequency map was employed for each city, and these 13 frequency maps were gathered into one map that was composed of the three strata. We selected 50 random pixels from the stable urban stratum, 50 random pixels from the stable non-urban stratum, and 100 sample pixels from the likely change stratum, resulting in a total of 200 pixel locations and 7000 pixel-year pairs for interpretation over the 35 years (1985–2019) (Figure 5). This procedure allowed us to follow the "good practice" guidance using a probability sampling design for estimating the area of land change [58]. The built-in Sampling Design Tool in ArcGIS was used to stratify the random samples [59]. Reference information was derived through examining and interpreting historical aerial images in Google Earth and Landsat imagery. We used Landsat false-color composites of SWIR-1, NIR, and RED, as well as various band combinations, which helped to increase the spectral separation and enhance the visual interpretation to differentiate the urban class from other land cover classes. Sample pixels were projected onto high-spatial-resolution Google Earth images to facilitate the interpretation of each site. When assessing the annual classifications, we labeled the reference sample pixels as either an urban or non-urban class in each year. To validate the change map, the reference sample pixels were labeled as one of three classes based on the status of each pixel over the 35 years: stable urban, stable non-urban, and urban change (which referred to a pixel that experienced urban expansion or urban shrinkage from 1985 to 2019).

Employing the methods that were reported by Olofsson et al. [60], we estimated the areas and uncertainties using the stratified sample. We also computed the overall, user's, and producer's accuracies, as well as the commission and omission errors. The variance

of the overall, user's, and producer's accuracies, as well as the confidence interval (95%) for each, were computed based on stratified random sampling using the method explained by Jenness and Wynne [61]. All of these computations were based on the estimated proportion of the error matrix and were conducted 35 times for each year between 1985 and 2019 when assessing the annual classification maps. We also conducted these computations when assessing the multi-temporal urban change map over the study period.

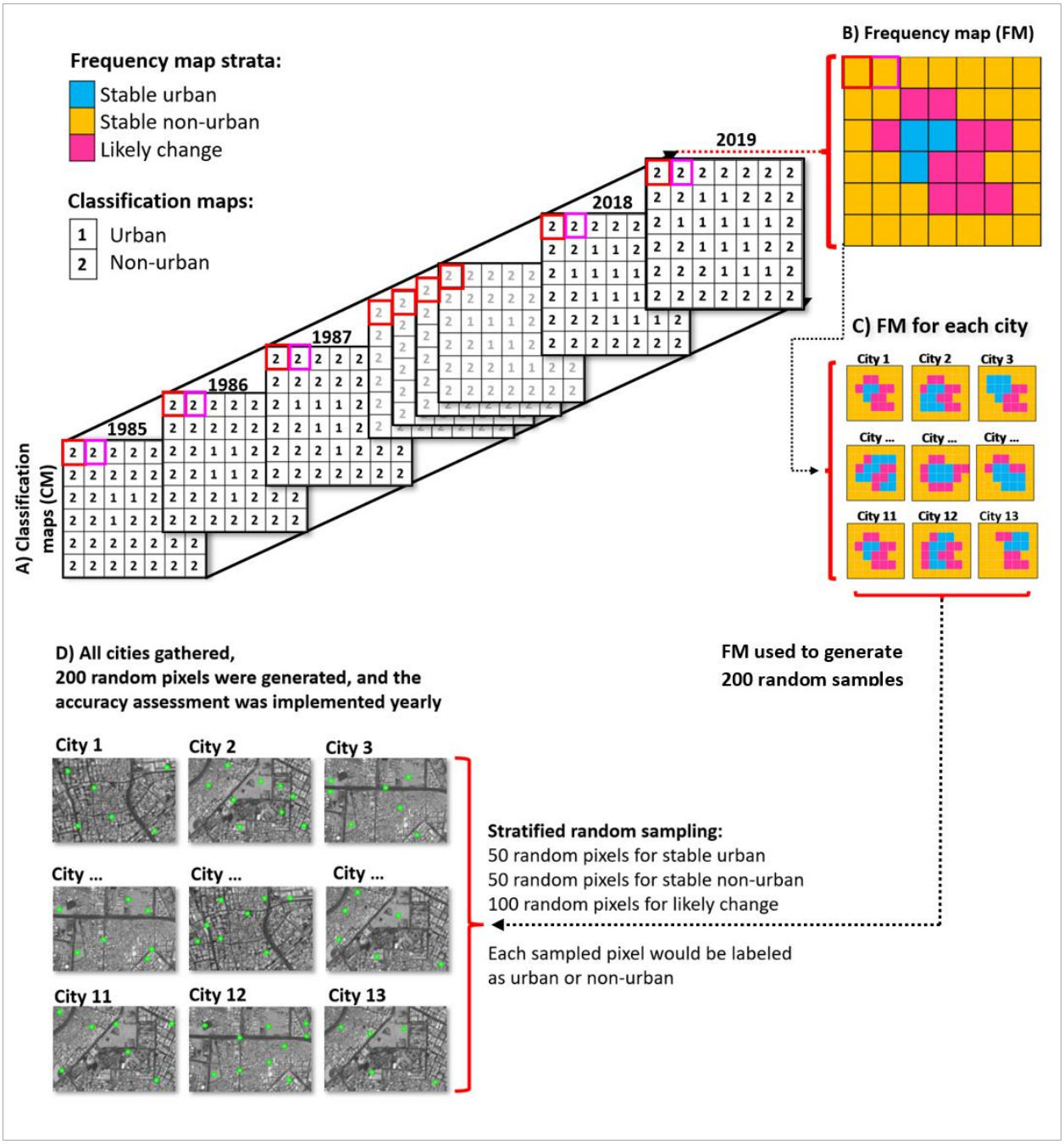

Figure 4. The process of accuracy assessment of the annual classification maps. Note: the green dots represent the random sampled pixels, and the black and white backdrop images represent the Landsat satellite images.

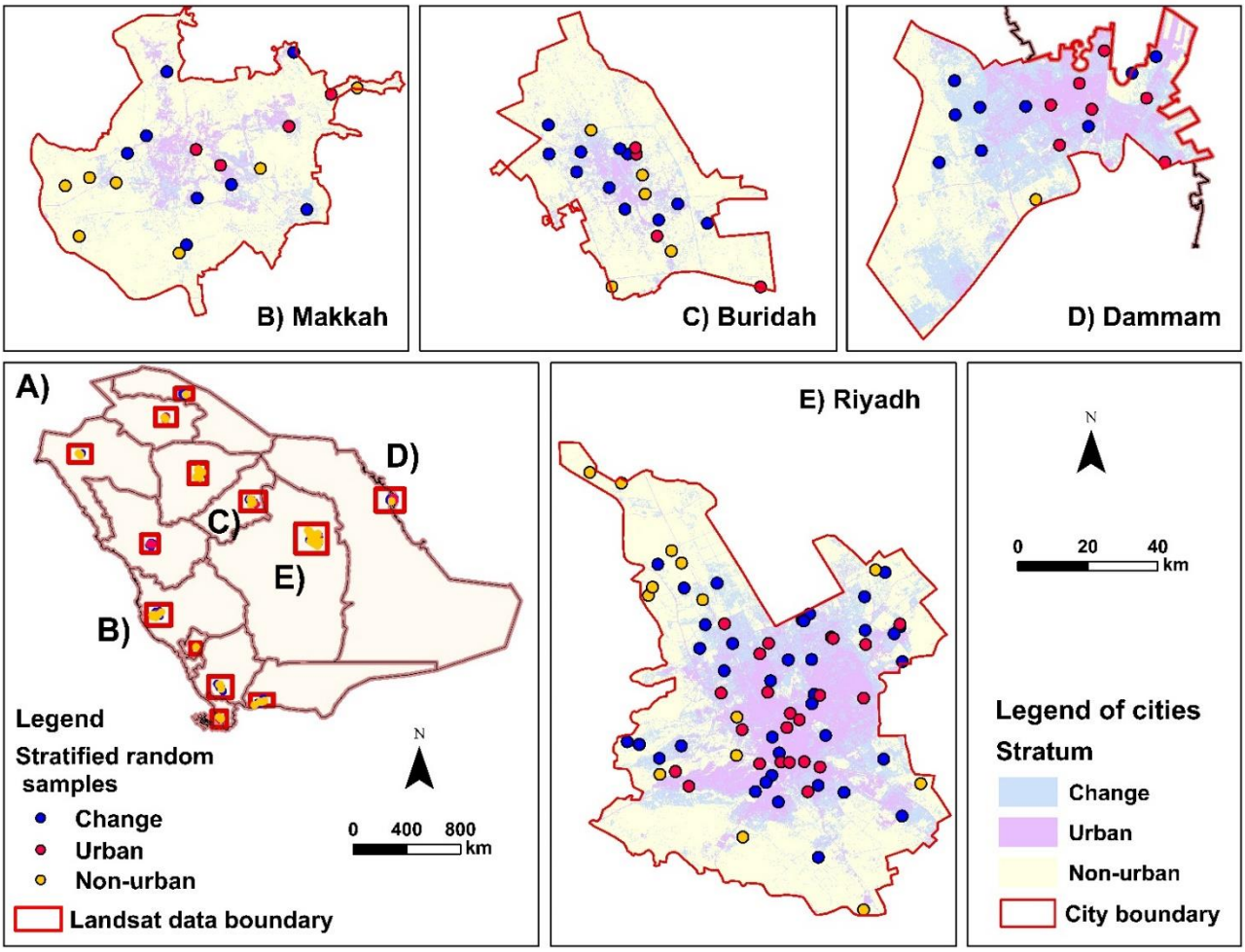

Figure 5. A map of Saudi Arabia (**A**) and the stratified random sampling design maps of four different capitals (**B**–**E**).

3.4. Estimating Urban Expansion Rate and Intensity (1985–2019)

To analyze the spatial and temporal characteristics of urban growth in the 13 Saudi cities between 1985 and 2019, we computed the urban expansion (km²) with two distinct indicators: urban expansion rate and expansion intensity. The urban expansion and intensity rate illustrate the dynamics within an urban area and quantify the expansion taking place. Hence, these two indicators contribute to the analysis of spatial changes in urban growth. The urban expansion is calculated by finding the difference in urban areas between two years. Once this is achieved, the rate of urban expansion U_e and urban expansion intensity U_i can be computed as follows [62]:

$$U_e = \frac{UA_{n+i} - UA_i}{UA_i} \times \frac{1}{n} \times 100 \quad (1)$$

$$U_i = \frac{\Delta UA_i}{TCA_i} \times \frac{1}{n} \times 100, \quad (2)$$

where UA is the urban area (km²), n is the interval of the calculation period (in years), i is the time, and TCA is the total city area (km²). Thus, in Equation (1), UA_{n+i} and UA_i are the urban areas in the target unit at times $n + i$ and i, respectively. In Equation (2), ΔUA_i is the difference between the urban areas at times $n + i$ and i. The rate of urban expansion is expressed as a percentage that was calculated by dividing the change of urban areas by the total urban areas throughout the specified study period, while the expansion intensity

is expressed as a percentage that was calculated by dividing the change of the urban area by the total city area unit. Although these indicators can be used to compare the quantities of the spatial characteristics of urban expansion over the study period, in this research, we computed these indicators for every five years for each city.

4. Results

4.1. Accuracy Assessments and Unbiased Area Estimations

We separated and quantified the errors by evaluating the accuracy of the annual classification maps for the urban and non-urban classes. Due to the similarity of the spectral responses between urban and barren lands and the complexity of mapping semi-arid and arid environments, the commission and omission errors were found to vary between the two classes. The commission errors for the urban class ranged between 2.29 and 18.75%, while the omission errors were between 4.42 and 19.63%. For the non-urban class, the errors of commission experienced a decline, with a range between 0.69 and 6.10%, while the omission errors were between 0.74 and 2.81%. In addition, the user's accuracies for the non-urban class increased over the period and were between 93.90 and 99.26%, while the user's accuracies for the urban class were between 81.25 and 99.26%. The producer's accuracies of the non-urban class were between 97.17 and 99.26%, while the accuracies for the urban class were between 80.37 and 95.52%. The overall accuracy was higher between 1985 and 2019, ranging between 93.21 and 98.09% (Figure 6).

Based on the stratified random sample, urban and non-urban areas were estimated once per year over the period 1985–2019 for a total of 35 times. The urban area rapidly increased over this period. In 1985, the urban area covered a total of 1305.28 ± 348.71 km^2 (the ± value represents the 95% confidence interval). In 2000, the urban area had continued to grow to around 1475.42 ± 336.75 km^2, and by 2019, the urban area had drastically increased to 2704.94 ± 554.04 km^2. The urban area represented 13.23, 14.96, and 27.43% of the total areas in 1985, 2000, and 2019, respectively. The non-urban area decreased over the same period (1985–2019) (Figure 7). For example, in 1985, the non-urban class covered a total of 8568.29 ± 543.96 km^2. In 2000, it covered 8399.36 ± 608.37 km^2, and by 2019, it totaled 7347.37 ± 1013.44 km^2. The non-urban area covered 86.89, 85.18, and 74.51% of the total areas in 1985, 2000, and 2019, respectively. These urban and non-urban areas have witnessed drastic changes, especially between 2000 and 2019. In urban areas, the general trend was a substantial increase, and there was a decrease in non-urban areas.

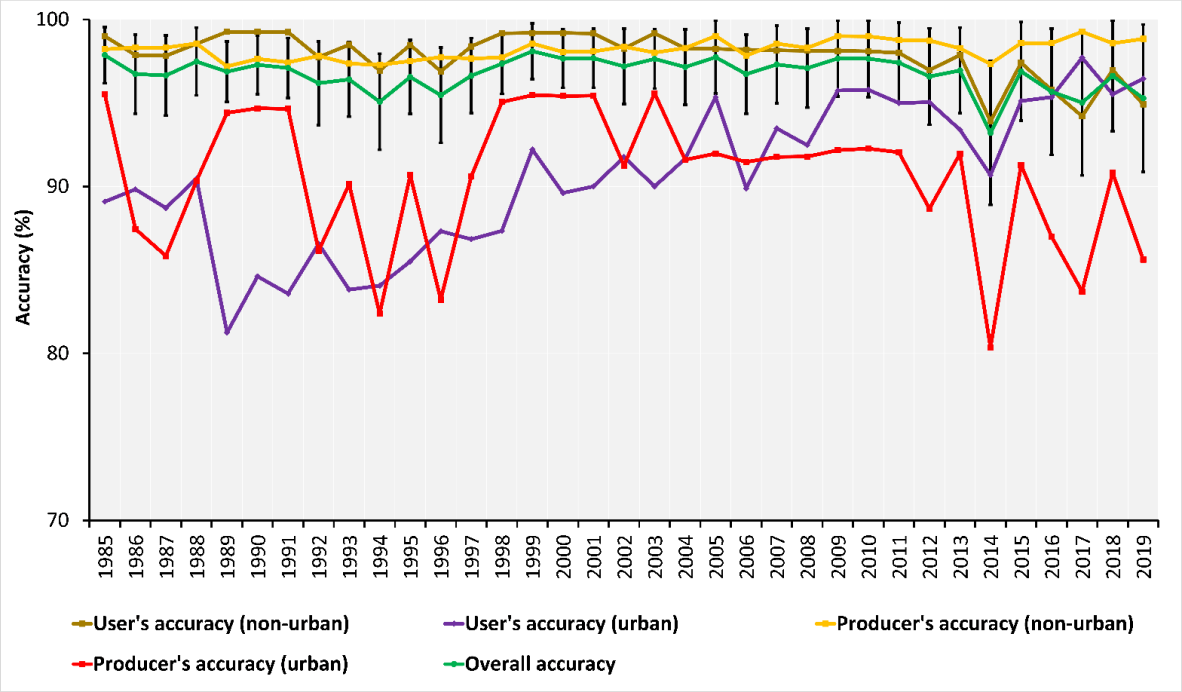

Figure 6. The user's, producer's, and overall accuracies from 1985 to 2019 (95% confidence intervals are represented by the error bars for overall accuracy).

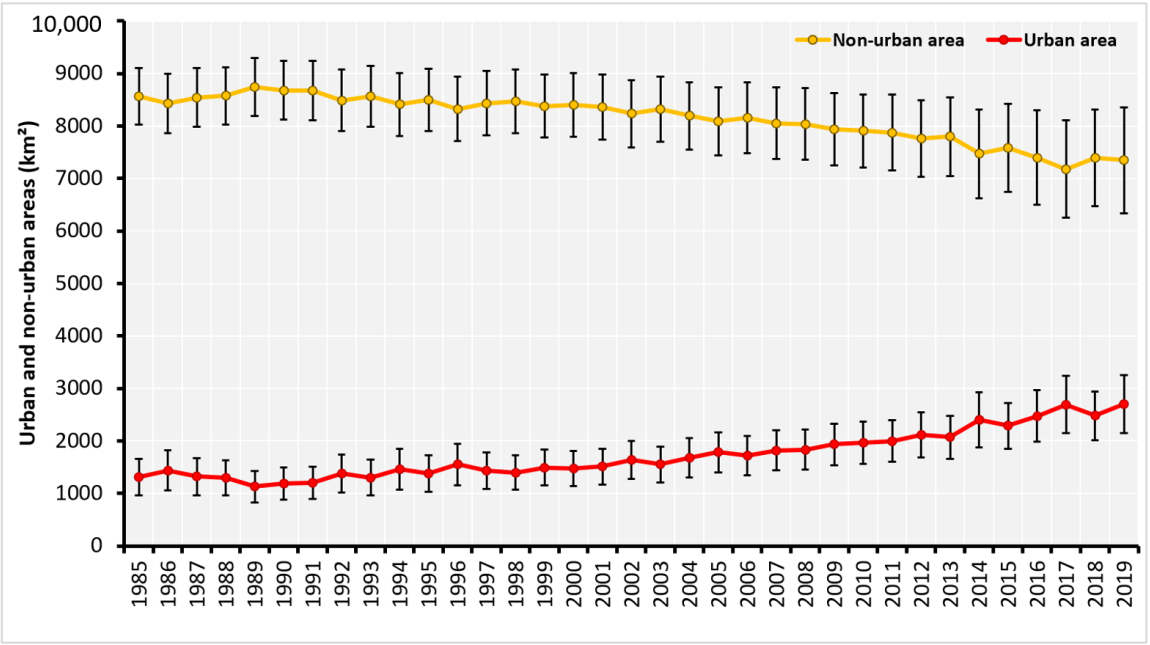

Figure 7. Unbiased urban and non-urban area estimates from 1985 to 2019 (95% confidence intervals are represented by the error bars).

We also quantified and evaluated the errors of the multi-temporal urban change map based on the sample. The user's and producer's accuracies varied between the three classes, ranging from 68 to 97% (Table 2). The producer's accuracy of the change class showed the lowest accuracy among the classes at 68%. The urban class showed the lowest user's accuracy at 76%. This lower accuracy was the result of the inter-annual variability. Even with the lower accuracy in some classes, the overall accuracy of the change map was high, reaching 91%. The change class area was large, approximately 2064.075 ± 571.663 km² (the ± value represents the 95% confidence interval). Overall, this assessment

illustrated the variation between the urban and non-urban pixels in arid and semi-arid environments.

Table 2. Confusion matrix of the multi-temporal urban change map (1985–2019).

		Reference Data			
		Stable Non-Urban	**Stable Urban**	**Change**	**Total**
Classified map	Stable non-urban	0.685	0.000	0.044	0.728
	Stable urban	0.002	0.083	0.024	0.109
	Change	0.018	0.003	0.141	0.162
	Total	0.705	0.086	0.209	1.000
	Area (km²)			2064.075	
	± 95% CI (km²)			571.663	
	User's accuracy	0.94	0.76	0.87	
	Producer's accuracy	0.97	0.96	0.68	
	Overall accuracy	0.91			

4.2. Characteristics of Urban Growth in Saudi Capital Cities (1985–2019)

4.2.1. Urban Expansion Rate and Intensity

We calculated the urban expansion, rate of urban expansion (U_e), and expansion intensity (U_i) to identify the urban growth trends in the capital cities over the 35 years. The expansion intensity was classified into six classes: high-speed expansion ($U_i > 1.92$), fast-speed expansion ($1.05 \le U_i \le 1.92$), medium-speed expansion ($0.59 \le U_i \le 1.05$), slow-speed expansion ($0.28 \le U_i \le 0.59$), slow expansion ($0 \le U_i \le 0.28$), and no expansion [63]. The variables of each indicator were extracted from the statistics that were derived from the outcome of the CCDC classification maps. The urban expansion (km²), urban expansion rate (%), and expansion intensity (%) were then identified and quantified for the 13 capital cities in Saudi Arabia (Figure 8).

The calculations of all three indicators revealed trends in the spatial and temporal heterogeneity of each city between 1985 and 2019, which was then divided into five-year intervals. In Riyadh, Dammam, Tabuk, Jazan, and Abha, the urban expansion and intensity reached 98.5 km² (0.79%), 42.43 km² (1.51%), 9.12 km² (0.49%), 8.83 km² (0.62%), and 4.81 km² (0.1%), respectively, and the urban expansion, urban expansion rate, and expansion intensity were significantly higher in the first interval (1985–1989). In addition to this increase, Riyadh, Buridah, Ha'il, Makkah, Arar, and Abha also showed substantial expansions and intensities in the last two intervals (2010–2014 and 2015–2019). For example, in the last interval (2015–2019), Riyadh, Dammam, Makkah, Buridah, and Ha'il had the highest urban expansions and expansion intensities at about 65.52 km² (0.52%), 25.29 km² (0.9%), 21.42 km² (0.38%), 19.21 km² (0.45%), and 16.99 km² (0.33%), respectively.

The urban expansion rates in Ha'il, Jazan, Dammam, and Tabuk (10.49, 10.63, 7.84, and 9.95%, respectively) denoted substantial increases in the first interval (1985–1989). Additionally, in the last interval (2015–2019), Arar, Abha, and Ha'il witnessed increases with rates above 3.1%. Though some of the capitals witnessed a major increase over the first and last intervals, the three indicators also showed a decrease in certain cities during the first and middle intervals, especially between 1985 and 2009. For instance, Madinah, Arar, Skakah, Buridah, and Najran each saw a decrease in growth with urban expansion at less than 3 km² and an urban expansion rate and intensity below 1%. There was a noticeable increase in urban expansion, urban expansion rate, and urban intensity in all 13 capitals during the sixth interval (2010–2014), which did not occur during any of the other intervals that were included in the study. This distinct growth was the result of an economic boom that occurred in Saudi Arabia during this period.

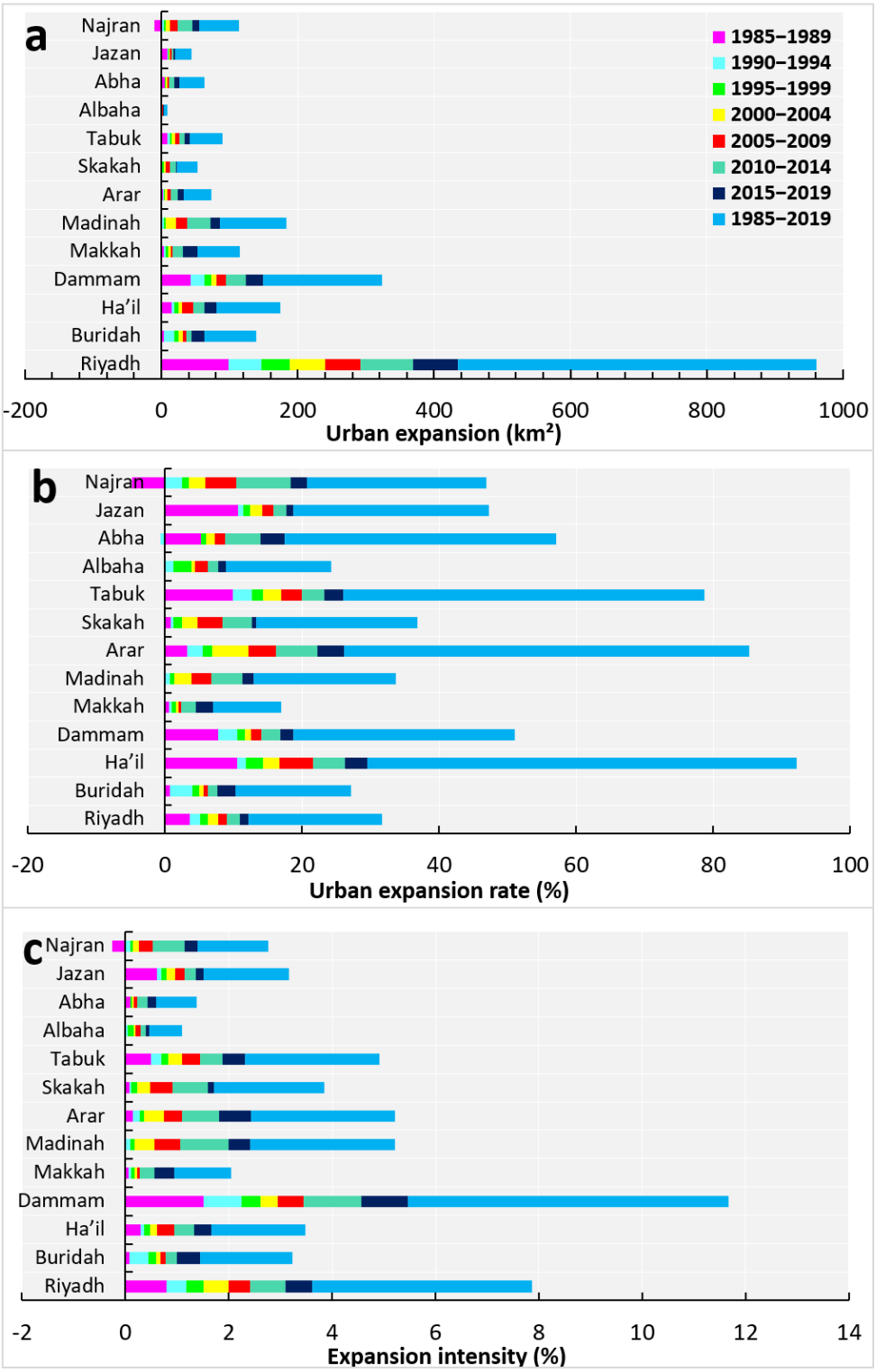

Figure 8. Three urban indices of the 13 capital cities (1985–2019): (**a**) urban expansion (km²), (**b**) urban expansion rate (%), and (**c**) expansion intensity (%).

4.2.2. Spatial and Temporal Analysis for the 13 Capital Cities

The change maps provide a visual representation of the land use and land cover changes that occurred in each of the capitals from 1985 to 2019 (Figure 9). Within the change maps, urban growth was tracked using a color scale that ranged from black for 1985 to dark red for 2019. The grey color represents the non-urban class. The urban expansion that is represented in each of the maps reveals distinct urban growth patterns

that are unique to each of the capitals and have varied over time. Tracking these data over the 35 years provided detailed spatial and temporal information about each city and represents a synoptic view of the urban growth in each regional capital.

The direction of urban growth was disparate for each city and depended on different factors, such as the topography, transportation networks, proximity to coastal areas, and city boundaries. Overall, Ha'il, Madinah, Makkah, Albaha, Abha, and Najran were found to have urban expansion patterns that were unique due to the influence of each city's topography. In contrast, Arar and Riyadh had uniform patterns that expanded in all four directions due to the ease of the surrounding terrain and the abundance of transportation networks. Urban growth in Tabuk was found to expand in specified directions due to the city's boundary, while Jazan and Dammam expanded to the east and west, respectively, because of their proximity to the Red Sea and Arabian Gulf, respectively.

Each city had a unique pattern of urban growth (Figure 9). For example, Tabuk, Skakah, and Arar are located in the northern region. The change map of Tabuk clearly illustrates the outward expansion of urban areas from the core of the city toward the north, east, and west along the transportation network, while the urban growth in the south was limited due to the city's boundary. Skakah was found to have experienced a slower rate of growth than Tabuk, with the majority of development occurring along the transportation network. Arar witnessed dramatic growth in all directions since there were no barriers to expansion.

The three capitals in the central region of Saudi Arabia are Ha'il, Buridah, and Riyadh. Ha'il was found to grow to the north, south, and east. Buridah, which is primarily agricultural, only experienced development in the north and southeast areas of the city. Riyadh experienced development in the north, south, and west of the city. This growth occurred most often near transportation networks and in areas where services were available to city inhabitants. In the eastern region, Dammam witnessed significant growth to the west and southwest of the city and limited growth in the east due to the barrier formed by the Arabian Gulf. In the western region of Saudi Arabia, Madinah extended mostly to the south and east rather than the north and west. Growth in Makkah mostly occurred to the south and east, while growth to the north and west was restricted by the city's topography.

Albaha, Abha, Najran, and Jazan are all located in the southern region of the country. Albaha, Abha, and Najran are also hindered by the surrounding topography, further demonstrating the role that topography plays in shaping the growth of urban areas. Growth in Albaha took the form of curves that extended to the north, east, and west. Najran was shown to have a unique urban pattern that longitudinally extended to the south and east along easy terrain, while the north and west are constrained by mountainous topography. As with the other capitals, the majority of this urban expansion was found to be near transportation and available services. Jazan, a coastal city, showed a small amount of growth to the east and along the coastal areas to the north and south.

The temporal patterns of urban growth varied from city to city depending on different socioeconomic, political, and cultural factors. Overall, the majority of growth occurred in recent years rather than in the earlier years of the study. For example, because Riyadh is the capital of both the Riyadh region and the country, it saw the largest amount of growth of all 13 capitals. This urban expansion increase began in 1997 and accelerated even further between 2009 and 2019. The bulk of Dammam's urban growth occurred between 1997 and 2019. The majority of growth in Abha, Najran, and Jazan took place between 2000 and 2019.

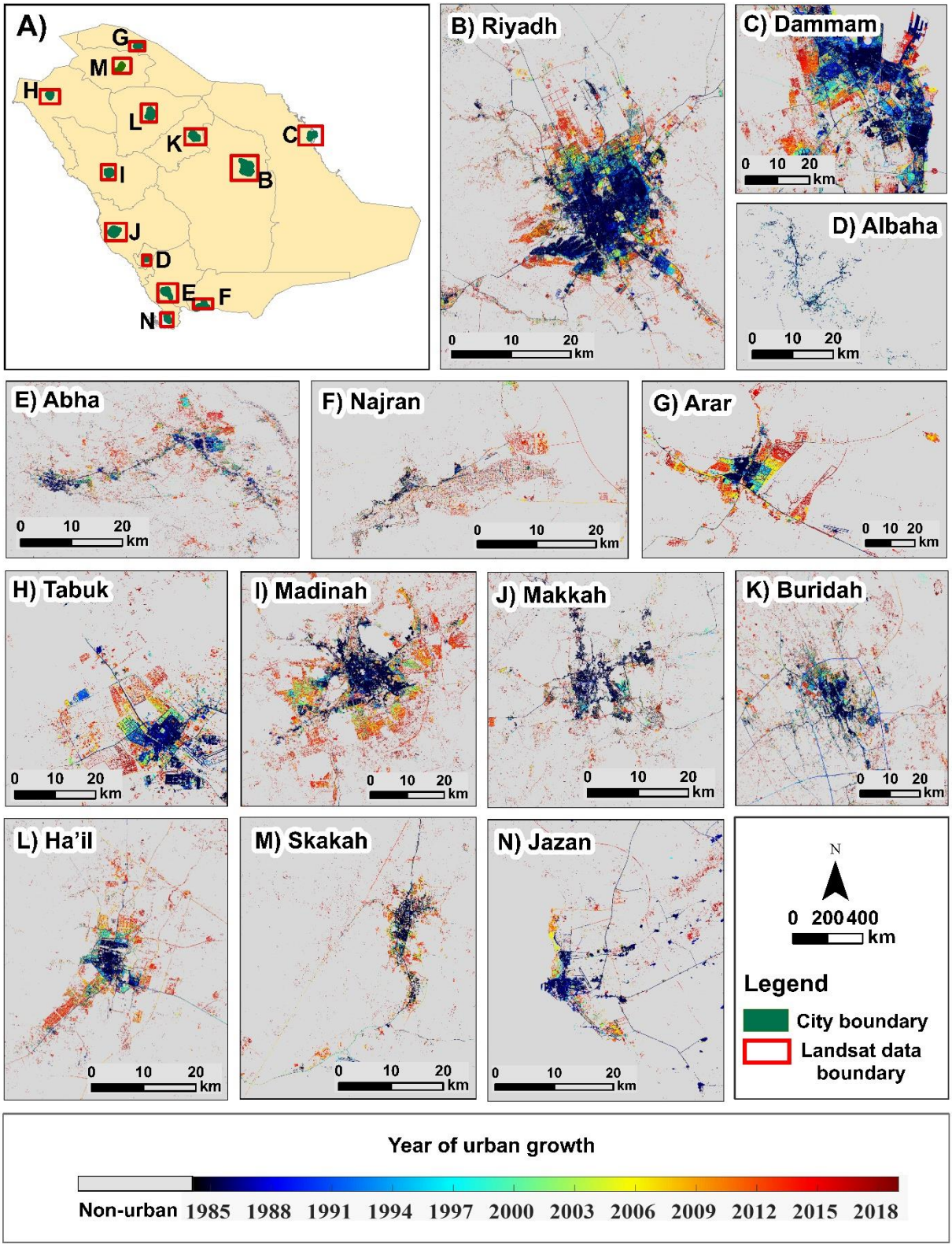

Figure 9. A map of Saudi Arabia (**A**) and multi-temporal urban change maps for all 13 capitals (**B**–**N**).

Three urban growth types were visually identified at the city level for each of the 13 capital cities: infilling, edge development, and leapfrogging (also known as outlying). The

infilling urban growth type occurs on vacant or undeveloped land within an existing community. In contrast, edge development occurs when the development of vacant or undeveloped land occurs along the periphery of developed areas. Leapfrogging occurs in sites that are near developed areas but not adjacent [64]. The most dominant urban growth type in most capital cities was found to be edge development, with infilling and leapfrogging present but limited. In Tabuk, Skakah, Arar, Ha'il, Riyadh, Dammam, Makkah, Madinah, and Najran, edge development was revealed to be the most common type of urban expansion, while leapfrogging and infilling were revealed to be the least common. Leapfrogging was the most dominant in Buridah, Albaha, Abha, and Jazan.

4.2.3. Examples of Riyadh, Dammam, and Arar

Based on the classification maps, we selected Riyadh, Dammam, and Arar to use as examples based on their total area to provide a representation of urban growth in a variety of city sizes. As Riyadh is the capital of Saudi Arabia and the Riyadh region, the city witnessed rapid growth along the entirety of its borders (Figure 10). Based on the classification maps, the urban areas covered about 540.63 km^2 (21.85%) in 1985 and 1067.05 km^2 (43.12%) in 2019. Urban areas had increased to almost double what they were in 1985. Most of this general urban growth was found to be clustered around transportation networks and services. In contrast, the non-urban areas dramatically decreased, falling from 1933.98 km^2 (78.15%) in 1985 to 1407.46 km^2 (56.88%) in 2019. Location B was a clear example of this infilling urban growth type. Between 2007 and 2019, edge expansion became the most common urban growth type, and it was distributed in the northern, western, and southern areas of the city along established transportation networks. Locations A, C, and D were examples of this edge expansion urban growth type. The leapfrogging urban growth type was never dominant and was limited to small areas that were located in the north, east, and south.

Dammam is located in one of the richest regions of Saudi Arabia due to massive petroleum resources (Figure 11). As such, the city experienced rapid growth between 1985 (108.22 km^2—19.27% of the total area) and 2019 (282.73 km^2—50.35% of the total area), indicating that Dammam witnessed an acceleration in urban growth. At the same time, non-urban areas experienced a dramatic decrease, going from 453.48 km^2 (80.76%) in 1985 to 277.58 km^2 (49.45%) in 2019. However, unlike Riyadh's growth, the expansion of urban areas in Dammam was mostly restricted to the west. This was because Dammam sits on the coast of the Arabian Gulf in the east and is bordered by Saihat in the north and Alkhobar and Dhahran in the south. These geographic constraints were made clear by the multi-temporal urban change that mostly extended to the west and was illustrated by the expanse of orange and red color in that area of the map compared with isolated pockets of yellow and red in the east. The infilling urban growth type was common within the city between 1994 and 2006, especially near the city's core. However, the edge expansion urban growth type was dominant between 1995 and 2019, especially on the western side of the city. The leapfrogging urban growth type was found to be limited to small areas throughout the different periods. Location A was an example of the infilling growth type, and locations B, C, and D were examples of the edge expansion growth type. The general urban growth pattern was revealed to be a combination of (mostly) clusters and (partially) dispersed growth.

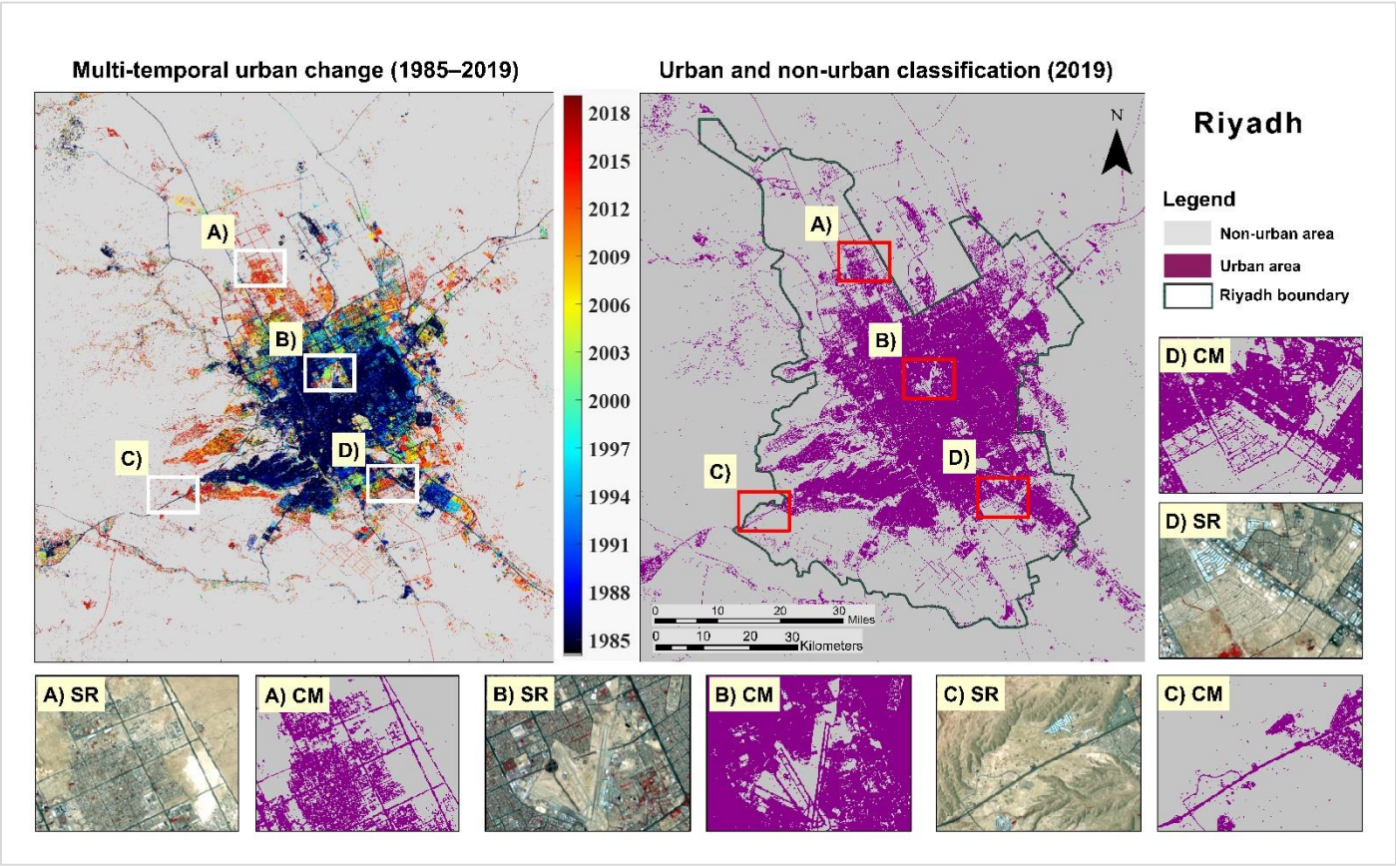

Figure 10. Multi-temporal urban change map (1985–2019) and urban and non-urban classifications in 2019 in Riyadh. Both include surface reflectance (SR) and classification map (CM) samples.

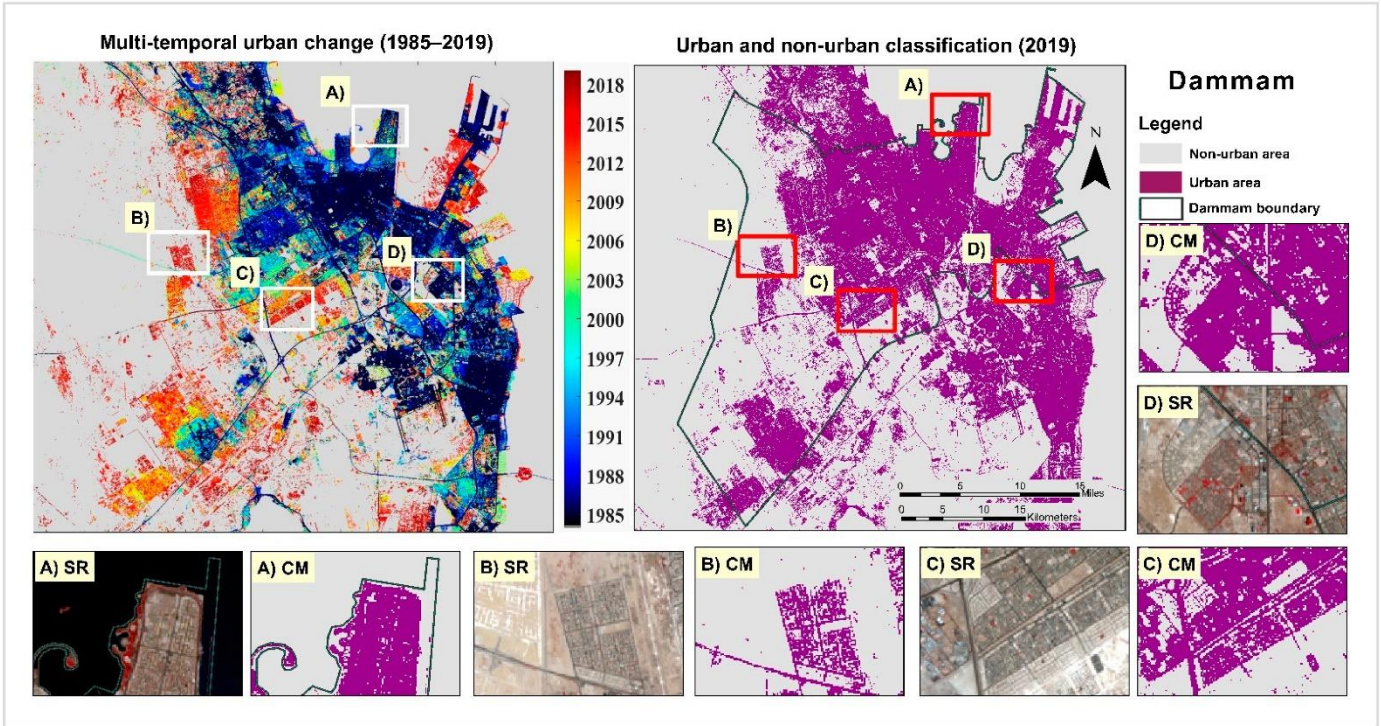

Figure 11. Multi-temporal urban change map (1985–2019) and urban and non-urban classifications in 2019 in Dammam. Both include surface reflectance (SR) and classification map (CM) samples.

Arar is the capital of the Aljawf and witnessed sluggish growth between 1985 and 2019 (Figure 12). Urban growth in Arar covered 13.94 km² (4.70%) in 1985 and increased threefold to approximately 55.16 km² (18.61%) in 2019. This growth rate was due to many factors, such as the city's population, the total area of the city, and human activities. However, the urban areas continuously grew near transportation networks and existing services. The detection maps revealed that the general pattern of urban growth in Arar was clustered. In 1985, Arar's non-urban area covered about 282.73 km² (95.37%) and decreased to about 141.20 km² (81.37%) in 2019. The infilling growth type between 1991 and 1995 was concentrated in the center of the city, whereas the edge expansion urban growth type grew gradually to the north, south, east, and west sides of the city, as indicated by the color change. The leapfrogging urban growth type was almost non-existent in the city. Locations A, B, C, and D exemplified the edge expansion type in Arar city.

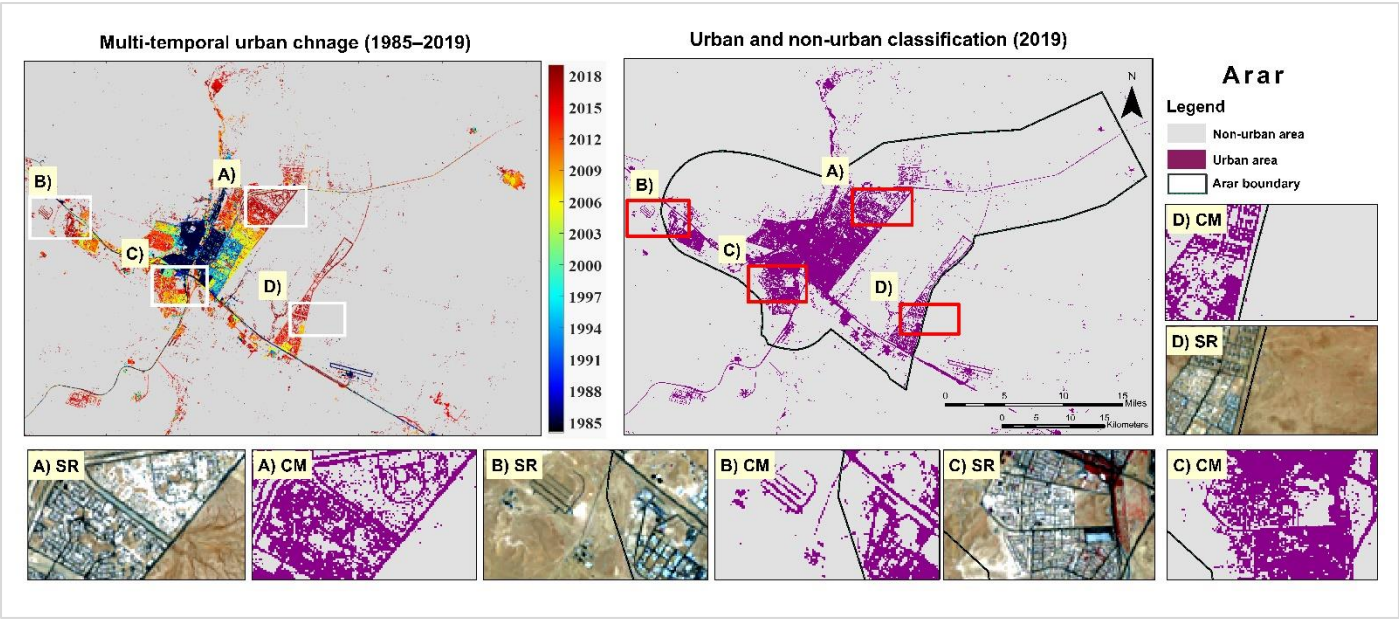

Figure 12. Multi-temporal urban change map (1985–2019) and urban and non-urban classifications in 2019 in Arar. Both include surface reflectance (SR) and classification map (CM) samples.

5. Discussion

This research provided the first quantitative examination of urban growth in Saudi Arabia's 13 capital cities. Growth in the capitals was tracked over 35 years (1985–2019), which generated a synoptic view of urban growth and provided specific data on the patterns, trends, and rates of urban expansion in each capital. This study showed that the Saudi capitals encountered massive urban growth between 1985 and 2019 and, according to all indicators, will continue to expand in the coming years. These results support arguments made by Alqurashi et al. [65], which claimed that cities in Saudi Arabia had experienced significant urban growth over the last four decades.

The combination of remotely sensed data and socioeconomic variables enables us to understand the interaction of the time series between urban growth and socioeconomic variables. The population size and the gross domestic product (GDP) are considered the main drivers of this growth. As the total population of Saudi Arabia has experienced an immense increase of 500% between 1974 and 2019 [30], and the urban area of Saudi capitals in 2019 (2704.94 ± 554.04 km²) was double that of 1985 (1305.28 ± 348.71 km²) (±values represent the 95% confidence intervals), it is essential to investigate the dynamic of population and urban growth in these cities in Saudi Arabia. We have examined the association between urban growth and population during the years: 1992, 2004, 2010, and

2017. Figure 13 highlights a positive correlation between urban growth and population size during the years listed (1992, 2004, 2010, 2017) in each Saudi capital, which was above 74%. The expansion in the capitals varied between fast and slow expansion over time. For example, Riyadh, Dammam, Buridah, and Ha'il have witnessed a solid increase, while Abha and Jazan have shown a sluggish increase during the four years. This increase indicates that the growing population plays a significant role in expanding the urban area in those capitals [40,66].

In addition, we have investigated the association between GDP and urban growth from 1985 to 2019. Figure 14 plots the urban area (km²) of all 13 capitals alongside the GDP of Saudi Arabia (in billions, USD) between 1985 and 2019 [67]. Even though there are some variations from year to year, the overall trend is that urban growth and GDP generally increased simultaneously. In detail, the prosperity or recession of the GDP influenced urban growth over time. For example, the stability of the GDP between 1991 and 1994 influenced the fluctuation of urban growth, as it only increased in a few capitals such as Tabuk, Dammam, and Riyadh, as shown in Figure 8. In contrast, the booming GDP had activated the increase in urban growth, as shown in Figures 8 and 13. The influence of population size and economic activities on urban growth, specifically increased demand for housing and providing subsidized mortgage loans for that housing, played a significant role in urban expansion in Saudi Arabia. The housing sector has undergone a tremendous change in recent years as the government has increased the subsidies to keep up with demand. According to the ministry of housing, in 2020, the housing sector experienced rapid growth and contributed more than 115 billion riyals to the GDP of the country (equivalent to 30.666 billion USD) [68]. Other factors influenced by a growing population include increases in urban areas, boosts in industrial production, and a higher total demand for energy. For example, Figure 15 plots the urban area (km²) of all 13 capital cities alongside the energy use of Saudi Arabia (kilogram of oil equivalent of energy) per USD 1000 in GDP (constant 2017 PPP) [69]. Even though there are some variations over time, including dramatic increases in energy consumption in 2002, 2010, and 2012, these two trends generally follow the same trajectory. Specifically, the correlation squared between urban areas and energy use showed a positive relationship (0.88), indicating that the energy use variable variation is attributed to the urban area variable.

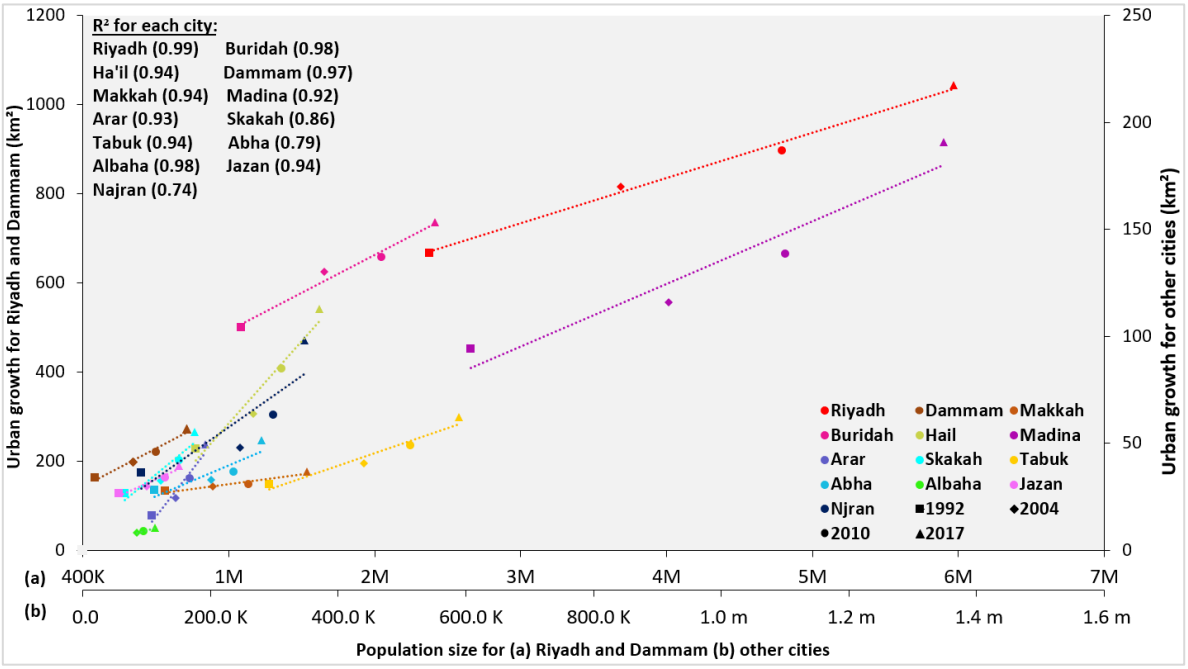

Figure 13. The trendline of urban growth and the population size.

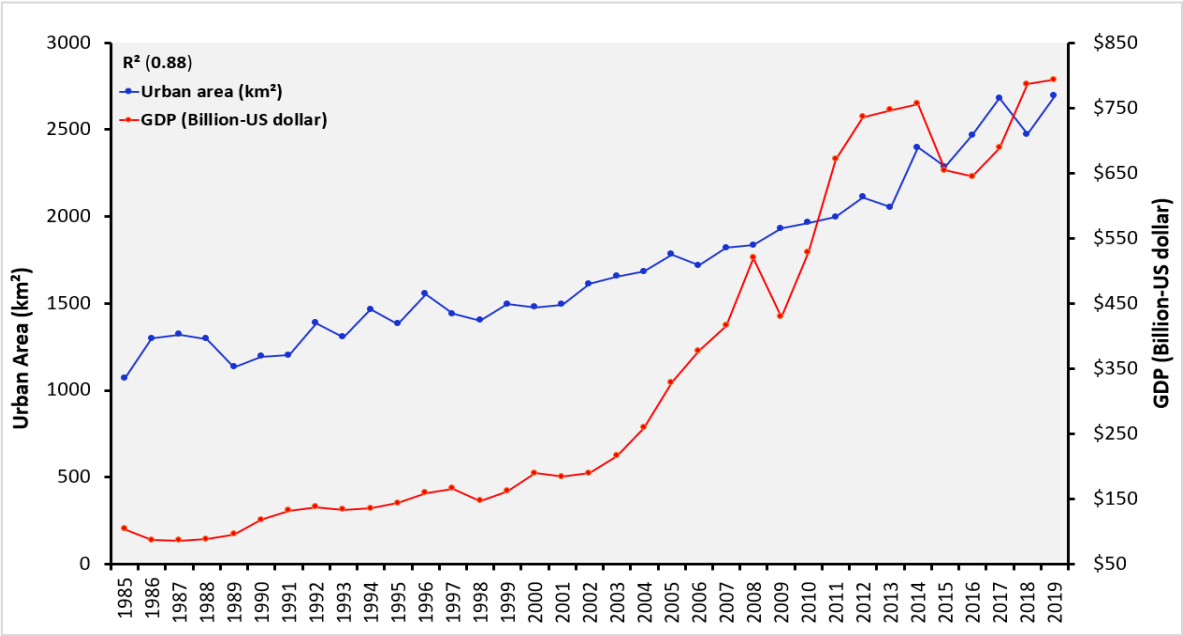

Figure 14. The urban area of the capitals and the GDP of the country.

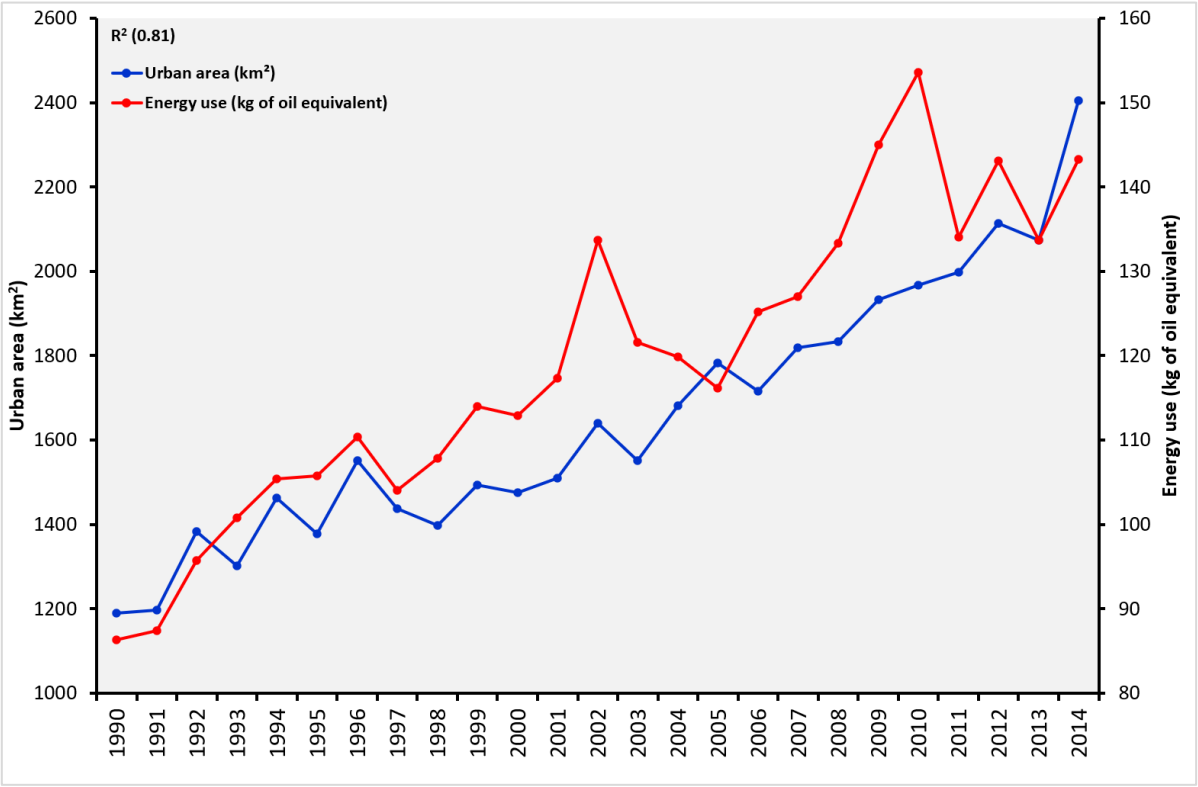

Figure 15. The urban area of the capitals and the energy use of the country.

Although this research provided information about the dynamics of urban growth in Saudi capital cities over the four decades, we encountered three major challenges: the complexity of mapping urban growth, the Scan Line Corrector (SLC) problem, and partially missing data in the classification maps. Mapping urban growth is challenging in semi-arid and arid environments due to the similarity of spectral signatures between urban and barren lands. Through our classification processes, agricultural lands presented as urban areas due to intra-annual changes that were caused by the vegetation

phenology that was propelled by environmental factors, such as climate variations. As result, we collected all possible training data that captured all relevant spectral heterogeneity between the classes to minimize this issue.

Numerous studies confronted the complexity of mapping arid and semi-arid environments and overcame these challenges using various specified image approaches. These approaches mitigated the misclassified errors and better discerned between urban and barren lands. For example, Aljaddani (2015) [38] classified and detected the urban growth in Jeddah city, Saudi Arabia, over three different years—1984, 2000, and 2013—using Landsat satellite images. The classified maps categorized the city into four classes: built-up area, barren land, vegetation, and water. Due to the difficulty of classifying the urban areas using spectral information alone, the texture was produced using the red band. Then, the red band texture was stacked into the visible, infrared, and near-infrared bands to classify the image. Our study illustrated the advantage of using this approach, as it produced higher overall accuracies for classification maps at between 96 and 97% in 1984, 2000, and 2013 compared with the conventional approach which produced an overall accuracy of between 88 and 91% for the same three years.

Another common issue that is found when mapping arid and semi-arid urban land cover is the mixed pixel and spectral confusion between impervious surfaces and bare soils. Zhang et al. (2015) [70] used a hybrid approach that comprised a linear spectral mixture analysis (LSMA), decision tree, and cluster analysis. This approach was implemented in arid and semi-arid cities—Urumqi, China, and Phoenix, USA—using the Landsat Thematic Mapper (TM). The LSMA approach unmixed the Landsat TM data into four endmember fraction images: high-albedo object, low-albedo object, vegetation, and bare soil. Then, new variables were extracted using these four endmember fraction images and added to the Landsat imagery to classify seven land use and land cover classes: forest, shrub, grass, crop, bare soil, impervious surfaces, and water. The authors illustrated that the approach showed the effectiveness of classifying and distinguishing urban land cover classes in arid and semi-arid environments. This approach was able to provide higher overall accuracy, with 86.0% for Urumqi and 88.7% for Phoenix compared with traditional maximum likelihood classification values of 65.3 and 72.3%, respectively.

Finally, using remote sensing indices to distinguish between urban areas and bare lands may perform better in humid regions than in dry regions [71]. For instance, Rasul et al. (2018) [71] developed two distinctive indices: dry built-up index (DBI) and dry bare-soil index (DBSI). The authors applied the DBI and DBSI using the Landsat Operational Land Imager (OLI-8) for 2013 in the city of Erbil, Iraq. The results illustrated that the indices provided higher overall accuracies of 93 and 92% for the DBI and DBSI, respectively, as well as illustrating the capability of the DBI and DBSI to distinguish between built-up areas and bare soils in dry regions. In agreement with the previously mentioned studies that focused on specified years, the development of a robust approach that uses time series is an important future investigation topic.

The second challenge was tied directly to the Scan Line Corrector (SLC). Despite the SLC producing data gaps in the form of lines in the Landsat ETM+ 7 images, the SLC-off mode still acquired about 78% of the data for any scene [72], which contributed significantly contributed to the CCDC algorithm and provided spatial and temporal information for the specified location. However, some Landsat ETM+ 7 images influenced the results of both the change detection and classification, which appeared in the form of thin, oblique lines that zigzagged along a horizontal plane in different locations. These lines were ultimately misclassified as an urban class in the classification maps. An in-depth investigation into the cause of this issue was a crucial part of this research that eventually allowed us to understand the source of misclassification and detect the images that triggered the anomaly. Several passes were required to remove all of these images. Once they were eliminated, we were able to reprocess the CCDC algorithm and produce change detection and classification maps that were free of distortion.

The third challenge involved data missing from the classification maps. The systematic, geometric, radiometric, and terrain elements of the Landsat data have to be corrected to deliver high-quality remotely sensed data to scientific users. Occasionally, Landsat data are influenced by anomalies and artifacts, such as data loss, impulse noise, banding, coherent noise, and internal calibrators [73]. Missing data in the time series of the satellite images affect the classification performance. In this research, after processing the CCDC algorithm, we found that some classification maps had missing pixels due to these anomalies and the artifacts that occurred due to the satellite sensors and atmospheric conditions. Some of the missing data had a unique shape, such as a building or agriculture circle, and some of them were randomly distributed between urban and agriculture, and mostly in barren lands. Due to the missing pixels only comprising a small percentage of the total area, near-date composite classification images were often a suitable solution to fill in the missing pixels. Different cities had different years of missing data in the classification maps. Some cities had larger amounts of missing data for a given year than others. The missing data within the boundaries of all 13 capitals were less than 5% and did not comprise a significant total in any of the maps generated for this study.

6. Conclusions

In this research, we presented methods and results regarding the long-term patterns and trends of urban growth in the 13 capital cities in Saudi Arabia. The research was accomplished by incorporating freely available Landsat images, the CCDC algorithm, and distinct expansion indices that assisted in providing a synoptic view of urban growth in the capitals as a whole and a detailed view of each city over 35 years. Assessing the accuracy of the annual classification maps and the multi-temporal urban change map and estimating the unbiased area helped to provide more reliable information about each city's overall growth. The results revealed that the urban area of Saudi capitals in 2019 (2704.94 ± 554.04 km^2) was double that of 1985 (1305.28 ± 348.71 km^2) (±values represent the 95% confidence intervals). We expect the urban expansion to continue in the near future, especially with the accelerated pace and diversity of current economic growth (especially in non-petroleum sectors), the increasing population, and the government's commitment to addressing the demand for residential, commercial, and industrial lands. In addition, policies in Saudi Arabia have changed to preserve the country's environment and ecosystem, which has led to Saudi cities becoming more sustainable. Thus, the availability of rich spatial and temporal information about historical urban growth can attribute to a better understanding of the dynamics of growth. Furthermore, delivering reliable annual long-term urban land cover maps over 35 years supports investigations into the current causes and consequences of these capitals' growth as well as helps predict the future of these capitals in certain socioeconomic and environmental scenarios. Examining these associations benefits the scientists, government institutions, private sectors, landowners, and policymakers as they address the outcomes of the enormous growth and establish policies to meet the sustainability of the capitals. Even though the authors of this research used the best possible method of collecting training data for each urban and non-urban area class, detecting and classifying urban growth were two of the main limitations of this study. New methods are needed to better understand and accurately map arid and semi-arid environments.

Author Contributions: Conceptualization, Z.Z.; methodology, Z.Z., X.-P.S., and A.H.A.; software, A.H.A.; validation, A.H.A.; formal analysis, A.H.A.; writing—original draft preparation, A.H.A.; writing—review and editing, X.-P.S., Z.Z., and A.H.A.; supervision, X.-P.S. All authors have read and agreed to the published version of the manuscript.

Funding: This research received no external funding.

Institutional Review Board Statement: Not applicable.

Informed Consent Statement: Not applicable.

Data Availability Statement: The *Saudi Arabian Capitals Urban Land Cover Maps: 1985–2019* dataset can be downloaded from [74] The code of the CCDC used in this study can be found in the GERS Lab from [75].

Acknowledgments: This research was performed using the High-Performance Computing Center (HPCC) at Texas Tech University, Lubbock, TX. We thank the anonymous reviewers for their insightful comments and suggestions, which assist in the improvement of our manuscript.

Conflicts of Interest: The authors declare no conflict of interest.

References

1. United Nations. *World Population Prospects 2017—Data Booklet (ST/ESA/SER.A/401)*; United Nations: New York, NY, USA, 2017.
2. Schneider, A.; Friedl, M.A.; Potere, D. Mapping global urban areas using MODIS 500-m data: New methods and datasets based on "urban ecoregions." *Remote Sens. Environ.* **2010**, *114*, 1733–1746. https://doi.org/10.1016/j.rse.2010.03.003.
3. Sun, J.; Wang, H.; Song, Z.; Lu, J.; Meng, P.; Qin, S. Mapping essential urban land use categories in nanjing by integrating multi-source big data. *Remote Sens.* **2020**, *12*, 2386. https://doi.org/10.3390/RS12152386.
4. United Nations World's Population Increasingly Urban with More Than Half Living in Urban Areas. Available online: https://www.un.org/en/development/desa/news/population/world-urbanization-prospects-2014.html (accessed on 2 January 2020).
5. Kirabo Kacyira, A. Addressing the sustainable urbanization challenge. *UN Chron.* **2012**, *49*, 58–60. https://doi.org/10.18356/f813137d-en.
6. Martine, G.; McGranahan, G.; Schensul, D.; Tacoli, C. *Population Dynamics and Climate Change*; UNFPA: New York, NY, USA, 2009; ISBN 9780897149198.
7. Seto, K.C.; Güneralp, B.; Hutyra, L.R. Global forecasts of urban expansion to 2030 and direct impacts on biodiversity and carbon pools. *Proc. Natl. Acad. Sci. USA* **2012**, *109*, 16083–16088. https://doi.org/10.1073/pnas.1211658109.
8. Seto, K.C.; Shobhakar, D.; Bigio, A.; Blanco, H.; Delgado, G.C.; Dewar, D.; Huang, L.; Inaba, A.; Kansal, A.; Lwasa, S.; et al. Human Settlements, Infrastructure, and Spatial Planning. In *Climate Change 2014: Mitigation of Climate Change Working Group III Contribution to the IPCC Fifth Assessment Report*; Cambridge University Press: Cambridge, UK, 2014; pp. 923–1000. https://doi.org/10.1017/cbo9781107415416.018.
9. Defries, R.S.; Rudel, T.; Uriarte, M.; Hansen, M. Deforestation driven by urban population growth and agricultural trade in the twenty-first century. *Nat. Geosci.* **2010**, *3*, 178–181. https://doi.org/10.1038/ngeo756.
10. Hahs, A.K.; McDonnell, M.J.; McCarthy, M.A.; Vesk, P.A.; Corlett, R.T.; Norton, B.A.; Clemants, S.E.; Duncan, R.P.; Thompson, K.; Schwartz, M.W.; et al. A global synthesis of plant extinction rates in urban areas. *Ecol. Lett.* **2009**, *12*, 1165–1173. https://doi.org/10.1111/j.1461-0248.2009.01372.x.
11. Hobbie, S.E.; Finlay, J.C.; Benjamin, D.; Nidzgorski, D.A.; Millet, D.B.; Lawrence, A.; Hobbie, S.E.; Finlay, J.C.; Janke, B.D.; Nidzgorski, D.A.; et al. Correction: Contrasting nitrogen and phosphorus budgets in urban watersheds and implications for managing urban water pollution. *Proc. Natl. Acad. Sci. USA* **2017**, *114*, 4177–4182. https://doi.org/10.1073/pnas.1618536114; Erratum in *Proc. Natl. Acad. Sci. USA* **2017**, *114*, E4116. https://doi.org/doi:10.1073/pnas.1706049114.
12. Liu, R.; Wang, M.; Chen, W.; Peng, C. Spatial pattern of heavy metals accumulation risk in urban soils of Beijing and its influencing factors. *Environ. Pollut.* **2016**, *210*, 174–181. https://doi.org/10.1016/j.envpol.2015.11.044.
13. Ying, Q.; Hansen, M.C.; Potapov, P.V.; Tyukavina, A.; Wang, L.; Stehman, S.V.; Moore, R.; Hancher, M. Global bare ground gain from 2000 to 2012 using Landsat imagery. *Remote Sens. Environ.* **2017**, *194*, 161–176. https://doi.org/10.1016/j.rse.2017.03.022.
14. Zhang, H.; Wang, S.; Hao, J.; Wang, X.; Wang, S.; Chai, F.; Li, M. Air pollution and control action in Beijing. *J. Clean. Prod.* **2016**, *112*, 1519–1527. https://doi.org/10.1016/j.jclepro.2015.04.092.
15. Peng, S.; Piao, S.; Ciais, P.; Friedlingstein, P.; Ottle, C.; Bréon, F.M.; Nan, H.; Zhou, L.; Myneni, R.B. Response to comment on "Surface urban heat island across 419 global big cities." *Environ. Sci. Technol.* **2012**, *46*, 6889–6890. https://doi.org/10.1021/es301811b.
16. Buchhorn, M.; Bertels, L.; Smets, B.; De Roo, B.; Lesiv, M.; Tsendbazar, N..; Masiliunas, D.; Linlin, L. *Copernicus Global Land Operations "Vegetation and Energy"*;"CGLOPS-1" Framework Service Contract N° 199494 (JRC) Algorithm Theoretical Basis Document Moderate Dynamic Land Cover Collection 100 M Version 3 Issue 3.4; Zenodo: Geneva, Switzerland, 2021. https://doi.org/10.5281/zenodo.3938968.PU.
17. Huang, X.; Huang, J.; Wen, D.; Li, J. An updated MODIS global urban extent product (MGUP) from 2001 to 2018 based on an automated mapping approach. *Int. J. Appl. Earth Obs. Geoinf.* **2021**, *95*, 102255. https://doi.org/10.1016/j.jag.2020.102255.
18. Friedl, M.A.; Sulla-Menashe, D.; Tan, B.; Schneider, A.; Ramankutty, N.; Sibley, A.; Huang, X. MODIS Collection 5 global land cover: Algorithm refinements and characterization of new datasets. *Remote Sens. Environ.* **2010**, *114*, 168–182. https://doi.org/10.1016/j.rse.2009.08.016.
19. Sulla-Menashe, D.; Gray, J.M.; Abercrombie, S.P.; Friedl, M.A. Hierarchical mapping of annual global land cover 2001 to present: The MODIS Collection 6 Land Cover product. *Remote Sens. Environ.* **2019**, *222*, 183–194. https://doi.org/10.1016/j.rse.2018.12.013.
20. Zhou, Y.; Smith, S.J.; Zhao, K.; Imhoff, M.; Thomson, A.; Bond-Lamberty, B.; Asrar, G.R.; Zhang, X.; He, C.; Elvidge, C.D. A global map of urban extent from nightlights. *Environ. Res. Lett.* **2015**, *10*, 054011. https://doi.org/10.1088/1748-9326/10/5/054011.

21. Bartholomé, E.; Belward, A.S. GLC2000: A new approach to global land cover mapping from earth observation data. *Int. J. Remote Sens.* **2005**, *26*, 1959–1977. https://doi.org/10.1080/01431160412331291297.
22. Bicheron, P.; Defourny, P.; Brockmann, C.; Schouten, L.; Vancutsem, C.; Huc, M.; Bontemps, S.; Leroy, M.; Achard, F.; Herold, M.; et al. GLOBCOVER Products Description Manual ESA GlobCover Project led by Medias France. Available online: https://publications.jrc.ec.europa.eu/repository/handle/JRC49240 (accessed on 15 January 2020).
23. *CIESIN Global Rural-Urban Mapping Project, Version 1 (GRUMPv1): Urban Extents Grid*; NASA Socioeconomic Data and Applications Center (SEDAC): Palisades, NY, USA. Available online: https://sedac.ciesin.columbia.edu/data/set/grump-v1-urban-extents (accessed on 15 January 2020).
24. Elvidge, C.D.; Tuttle, B.T.; Sutton, P.S.; Baugh, K.E.; Howard, A.T.; Milesi, C.; Bhaduri, B.L.; Nemani, R. Global distribution and density of constructed impervious surfaces. *Sensors* **2007**, *7*, 1962–1979. https://doi.org/10.3390/s7091962.
25. Schneider, A.; Friedl, M.A.; Potere, D. A new map of global urban extent from MODIS satellite data. *Environ. Res. Lett.* **2009**, *4*, 2000–2010. https://doi.org/10.1088/1748-9326/4/4/044003.
26. Florczyk, A.J.; Melchiorri, M.; Orbane, C.; Schiavina, M.; Maffenini, M.; Politis, P.; Sabo, S.; Freire, S.; Ehrlich, D.; Kemper, T.; et al. *Description of the GHS Urban Centre Database 2015*; Publications Office of the European Union: Luxembourg, 2019; p. 79. https://doi.org/10.2760/037310.
27. Small, C. A global analysis of urban reflectance. *Int. J. Remote Sens.* **2005**, *26*, 661–681. https://doi.org/10.1080/01431160310001654950.
28. Gong, P.; Li, X.; Wang, J.; Bai, Y.; Chen, B.; Hu, T.; Liu, X.; Xu, B.; Yang, J.; Zhang, W.; et al. Annual maps of global artificial impervious area (GAIA) between 1985 and 2018. *Remote Sens. Environ.* **2020**, *236*, 111510. https://doi.org/10.1016/j.rse.2019.111510.
29. Gong, P.; Li, X.; Zhang, W. 40-Year (1978–2017) human settlement changes in China reflected by impervious surfaces from satellite remote sensing. *Sci. Bull.* **2019**, *64*, 756–763. https://doi.org/10.1016/j.scib.2019.04.024.
30. Population and Housing Census. Available online: https://www.stats.gov.sa/en/13 (accessed on 15 January 2020).
31. Saudi Oil Production Policy. Available online: https://www.moenergy.gov.sa/arabic/ministry/Pages/petroleum-and-politics.aspx (accessed on 3 March 2020).
32. The Energy. Available online: https://www.moenergy.gov.sa/arabic/Energy/Pages/petroleum.aspx (accessed on 7 January 2020).
33. Abdelatti, H.; Elhadary, Y.; Babiker, A.A. Nature and Trend of Urban Growth in Saudi Arabia: The Case of Al-Ahsa Province—Eastern Region. *Resour. Environ.* **2017**, *7*, 69–80. https://doi.org/10.5923/j.re.20170703.02.
34. Alhowaish, A.K. Eighty years of urban growth and socioeconomic trends in Dammam Metropolitan Area, Saudi Arabia. *Habitat Int.* **2015**, *50*, 90–98. https://doi.org/10.1016/j.habitatint.2015.08.019.
35. Al-Shihri, F.S. Impacts of large-scale residential projects on urban sustainability in Dammam Metropolitan Area, Saudi Arabia. *Habitat Int.* **2016**, *56*, 201–211. https://doi.org/10.1016/j.habitatint.2016.06.001.
36. Aljoufie, M.; Zuidgeest, M.; Brussel, M.; van Maarseveen, M. Spatial-temporal analysis of urban growth and transportation in Jeddah City, Saudi Arabia. *Cities* **2013**, *31*, 57–68. https://doi.org/10.1016/j.cities.2012.04.008.
37. Jamali, N.A.; Rahman, M.T. Utilization of Remote Sensing and GIS to Examine Urban Growth in the City of Riyadh, Saudi Arabia. *J. Adv. Inf. Technol.* **2016**, *7*, 297–301. https://doi.org/10.12720/jait.7.4.297-301.
38. Aljaddani, A. Integration of Multi-Temporal Remote Sensing Imagery and GIS Mapping and Analysis of Land Use Change in Jeddah City, Saudi Arabia. Ph.D. Thesis, Murray State University, Murray, KY, USA, 2015.
39. Abdulrazzak, M.J. Water Supplies versus Demand in Countries of Arabian Peninsula. *J. Water Resour. Plan. Manag.* **1995**, *121*, 227–234. https://doi.org/10.1061/(asce)0733-9496(1995)121:3(227).
40. Saudi Census. Available online: https://www.stats.gov.sa/sites/default/files/population_by_age_groups_and_gender_ar.pdf (accessed on 15 January 2020).
41. Abdul Salam, A.; Elsegaey, I.; Khraif, R.; Al-Mutairi, A. Population distribution and household conditions in Saudi Arabia: Reflections from the 2010 Census. *Springerplus* **2014**, *3*, 1–13. https://doi.org/10.1186/2193-1801-3-530.
42. National Geological Database (NGD). Available online: https://ngd.sgs.org.sa/en (accessed on 10 August 2019).
43. Saeed, T.M.; Al-Dashti, H.; Spyrou, C. Aerosol's optical and physical characteristics and direct radiative forcing during a shamal dust storm, a case study. *Atmos. Chem. Phys.* **2014**, *14*, 3751–3769. https://doi.org/10.5194/acp-14-3751-2014.
44. Al Tokhais, A.S.; Rausch, R. The Hydrogeology of Al Hassa Springs. In Proceedings of the Third International Conference on Water Resources and Arid Environments (2008) and the First Arab Water Forum, Riyadh, Saudi Arabia, 16–19 November 2008.
45. Abha. Available online: https://unhabitat.org/sites/default/files/2020/05/abha.pdf (accessed on 15 January 2020).
46. Krishna, V. Long Term Temperature Trends in Four Different Climatic Zones of Saudi Arabia. *Int. J. Appl. Sci. Technol.* **2014**, *4*, 233–242.
47. U.S. Geological Survey. Available online: https://espa.cr.usgs.gov/ (accessed on 19 August 2019).
48. Masek, J.G.; Vermote, E.F.; Saleous, N.E.; Wolfe, R.; Hall, F.G.; Huemmrich, K.F.; Gao, F.; Kutler, J.; Lim, T.K. A landsat surface reflectance dataset for North America, 1990–2000. *IEEE Geosci. Remote Sens. Lett.* **2006**, *3*, 68–72. https://doi.org/10.1109/LGRS.2005.857030.
49. Vermote, E.F.; El Saleous, N.; Justice, C.O.; Kaufman, Y.J.; Privette, J.L.; Remer, L.; Roger, J.C.; Tanré, D. Atmospheric correction of visible to middle-infrared EOS-MODIS data over land surfaces: Background, operational algorithm and validation. *J. Geophys. Res. Atmos.* **1997**, *102*, 17131–17141.

50. Townshend, J.R.; Masek, J.G.; Huang, C.; Vermote, E.F.; Gao, F.; Channan, S.; Sexton, J.O.; Feng, M.; Narasimhan, R.; Kim, D.; et al. Global characterization and monitoring of forest cover using Landsat data: Opportunities and challenges. *Int. J. Digit. Earth* **2012**, *5*, 373–397. https://doi.org/10.1080/17538947.2012.713190.
51. Vermote, E.; Justice, C.; Claverie, M.; Franch, B. Preliminary analysis of the performance of the Landsat 8/OLI land surface reflectance product. *Remote Sens. Environ.* **2016**, *185*, 46–56. https://doi.org/10.1016/j.rse.2016.04.008.
52. Zhu, Z.; Wang, S.; Woodcock, C.E. Improvement and expansion of the Fmask algorithm: Cloud, cloud shadow, and snow detection for Landsats 4-7, 8, and Sentinel 2 images. *Remote Sens. Environ.* **2015**, *159*, 269–277. https://doi.org/10.1016/j.rse.2014.12.014.
53. Zhu, Z.; Woodcock, C.E. Object-based cloud and cloud shadow detection in Landsat imagery. *Remote Sens. Environ.* **2012**, *118*, 83–94. https://doi.org/10.1016/j.rse.2011.10.028.
54. Zhu, Z.; Woodcock, C.E.; Holden, C.; Yang, Z. Generating synthetic Landsat images based on all available Landsat data: Predicting Landsat surface reflectance at any given time. *Remote Sens. Environ.* **2015**, *162*, 67–83. https://doi.org/10.1016/j.rse.2015.02.009.
55. Zhu, Z.; Woodcock, C.E. Continuous change detection and classification of land cover using all available Landsat data. *Remote Sens. Environ.* **2014**, *144*, 152–171. https://doi.org/10.1016/j.rse.2014.01.011.
56. Anderson, J.; Hardy, E.; Roach, J.; Witmer, R. *A Land Use and Land Cover Classification System for Use with Remote Sensor Data*; US Government Printing Office: Washington, DC, USA, 1976; Volume 964.
57. Breiman, L. Random forests. In *Hands-On Machine Learning with R*; Chapman and Hall/CRC: London, UK, 2001; pp. 1–122. https://doi.org/10.1201/9780367816377-11.
58. Olofsson, P.; Foody, G.M.; Herold, M.; Stehman, S.V.; Woodcock, C.E.; Wulder, M.A. Good practices for estimating area and assessing accuracy of land change. *Remote Sens. Environ.* **2014**, *148*, 42–57. https://doi.org/10.1016/j.rse.2014.02.015.
59. Buja, K. Sampling Design Tool (ArcGIS 10.4.1). Available online: https://www.arcgis.com/home/item.html?id=28f08ca526ae44e8ac107a2a0d5f50e3 (accessed on 20 April 2020).
60. Olofsson, P.; Foody, G.M.; Stehman, S.V.; Woodcock, C.E. Making better use of accuracy data in land change studies: Estimating accuracy and area and quantifying uncertainty using stratified estimation. *Remote Sens. Environ.* **2013**, *129*, 122–131. https://doi.org/10.1016/j.rse.2012.10.031.
61. Jenness, J.; Wynne, J. *Cohen's Kappa and Classification Table Metrics 2.0: An ArcView 3x Extension for Accuracy Assessment of Spatially Explicit Models*; Southwest Biological Science Center Open-File Report; U.S. Geological Survey, Southwest Biological Science Center: Flagstaff, AZ, USA, 2005. https://doi.org/10.13140/RG.2.2.34549.40160.
62. Xu, X.; Min, X. Quantifying spatiotemporal patterns of urban expansion in China using remote sensing data. *Cities* **2013**, *35*, 104–113. https://doi.org/10.1016/j.cities.2013.05.002.
63. Chen, K.; Zhang, F.; Du, Z.; Liu, R. Analysis of urban expansion and driving forces in Jiaxing city based on remote sensing image. *J. China Univ. Min. Technol. China Univ. Min. Technol.* **2007**, *17*, 267–271. https://doi.org/10.3785/j.issn.1008-9497.2016.06.016.
64. Sun, C.; Wu, Z.F.; Lv, Z.Q.; Yao, N.; Wei, J.B. Quantifying different types of urban growth and the change dynamic in Guangzhou using multi-temporal remote sensing data. *Int. J. Appl. Earth Obs. Geoinf.* **2013**, *21*, 409–417. https://doi.org/10.1016/j.jag.2011.12.012.
65. Alqurashi, A.F.; Kumar, L.; Sinha, P. Urban land cover change modelling using time-series satellite images: A case study of urban growth in five cities of Saudi Arabia. *Remote Sens.* **2016**, *8*, 838. https://doi.org/10.3390/rs8100838.
66. Saudi Arabia-Major Cities. Available online: https://www.citypopulation.de/en/saudiarabia/cities/ (accessed on 9 September 2020).
67. The World Bank. Available online: https://data.worldbank.org/indicator/NY.GDP.MKTP.CD?locations=SA (accessed on 9 January 2020).
68. The Performance of the Housing Sector during the Corona Pandemic. 2020. Available online: https://hdoc.sa/en-us/Pages/NewsLetters.aspx (accessed on 20 February 2020).
69. The World Bank. Available online: https://data.worldbank.org/indicator/EG.USE.COMM.GD.PP.KD?locations=SA (accessed on 1 May 2022).
70. Zhang, C.; Chen, Y.; Lu, D. Mapping the land-cover distribution in arid and semiarid urban landscapes with Landsat Thematic Mapper imagery. *Int. J. Remote Sens.* **2015**, *36*, 4483–4500. https://doi.org/10.1080/01431161.2015.1084552.
71. Rasul, A.; Balzter, H.; Ibrahim, G.R.F.; Hameed, H.M.; Wheeler, J.; Adamu, B.; Ibrahim, S.; Najmaddin, P.M. Applying built-up and bare-soil indices from Landsat 8 to cities in dry climates. *Land* **2018**, *7*, 81. https://doi.org/10.3390/land7030081.
72. Chen, J.; Chen, J.; Liao, A.; Cao, X.; Chen, L.; Chen, X.; He, C.; Han, G.; Peng, S.; Lu, M.; et al. Global land cover mapping at 30 m resolution: A POK-based operational approach. *ISPRS J. Photogramm. Remote Sens.* **2015**, *103*, 7–27. https://doi.org/10.1016/j.isprsjprs.2014.09.002.
73. Landsat Known Issues. Available online: https://www.usgs.gov/land-resources/nli/landsat/landsat-known-issues (accessed on 10 July 2020).
74. Aljaddani, A.; Song, X.-P.; Zhu, Z. Saudi Arabian Capitals Urban Land Cover Maps: 1985–2019. Version: 1. Available online: https://zenodo.org/record/6210073#.Yn_bJ-jMKF4 (accessed on 21 February 2022).
75. Zhu, Z. GERSL–CCDC. Available online: https://github.com/GERSL/CCDC (accessed on 8 August 2019).